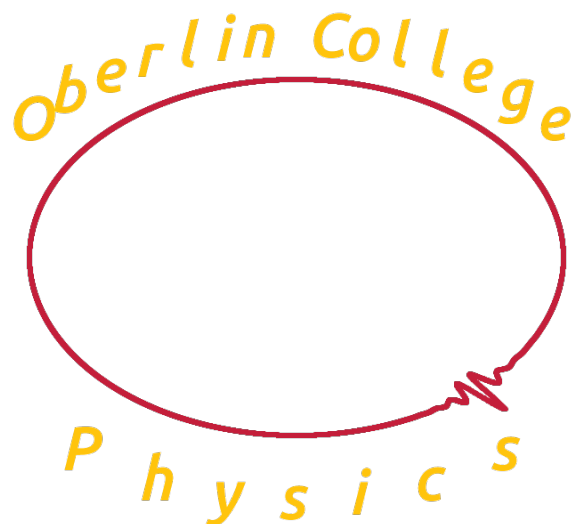


Unusual Magnetic Spin Arrangements in Manganese Ferrite Nanoparticle Assemblies



Ian Hunt-Isaak
Physics and Astronomy
Oberlin College

Submitted: March 31, 2017
Revised: May 16, 2017

Executive Summary

Magnetic nanoparticles have diameters of about 5-100 nm and exhibit magnetic properties that can differ dramatically from the bulk properties of the same material. These differences arise on account of the small size of the nanoparticles, the importance of surface effects, and internanoparticle interactions. Their unique properties have led to many current and proposed nanoparticle technologies in fields such as data storage, water decontamination, and targeted gene and drug delivery, with all of these applications requiring an understanding of the magnetic properties of the nanoparticles.

However, the small size of nanoparticles renders many traditional magnetometry methods ineffective as tools to understand magnetism on a nanoscale. In this thesis, we demonstrate the power of polarization analyzed small angle neutron scattering (PASANS) as a method to investigate the magnetic structure of manganese ferrite nanoparticles. Manganese ferrite was chosen as it is the natural continuation of previous work by Professor Ijiri, has potential uses in medicine and water decontamination, and has important differences in bulk properties from previously studied systems. The PASANS data reveal that individual nanoparticles partially align with an applied field, and unexpectedly, that the components of their magnetization perpendicular to the field are strongly correlated with neighboring nanoparticles. To fully explain the field and temperature dependence of the observed scattering data, we describe a model based on balancing the competing energy terms in a close packed hexagonal lattice of nanoparticles. The model captures the observed scattering data for conditions in which we expect small domains to form, and there are plans to extend its capabilities to allow for it to describe the data from field and temperature conditions with larger domain sizes. Taken together, the data and model underscore the importance of interparticle dipolar interactions in this system. Additionally, in order to arrive at these results, we had to develop new sample depolarization correction procedures, and created software tools to aid in the data treatment and analysis for future PASANS experiments, further extending the usefulness of the method.

Acknowledgments

This thesis would not have been possible without the many contributions of our collaborators. Professor Sara Majetich and her students, Samuel Oberdick and Ahmed Abdelgawad, from Carnegie Mellon University synthesized and performed initial characterization experiments on the manganese ferrite nanoparticle sample described here, also arranged for more sophisticated analysis as appropriate. Drs. Julie Borchers and Kathryn Krycka from the NIST Center for Neutron Research provided invaluable insights in the experimental neutron scattering data collection and analysis process. Drs. Wangchun Chen and Shannon Watson, also at NIST, provided essential assistance and development work in the ${}^3\text{He}$ cells needed for these unusual experiments. Hillary Pan and Jason Heitler-Klevans have been fantastic lab-mates and have both contributed directly to the work presented in this thesis. The National Science Foundation has provided support and funding for this work through DMR-1606887.

On a personal level, I am astounded upon reflection as to just how many people have played critical roles in my development as person, and as scientist. So many of the teachers and staff of my pre-college education were important to me, though none so much as Bob Schwartz. Without him, I and so many others might never have discovered a love of physics (and puns). Thanks also go to Master Kremin, and the entire AmKor family.

As a research advisor, Yumi Ijiri's incredible ability to know when to push, and when to give me space and freedom to explore has not gone unnoticed and I am deeply grateful for it. Jason Stalnaker, Stephen Fitzgerald, and Dan Styer have taught me nearly all of the physics I know, so I certainly would not have gotten here without them. I need to thank the rest of the Oberlin physics faculty and staff, in particular Diane Doman, for all they do to create an environment I truly enjoy being in. I deeply appreciate their care for me and all my classmates as people. Equally important in that environment have been all my fellow physics students. College wouldn't have been the same without you being there with me at 4 am working on a problem set.

All of my friends deserve thanks for exposing me to new things, and ideas,

and for having made my life to date a happy one. My family needs thanks for having instilled in me curiosity and so many other things in addition to having kept me alive when I was a toddler.

If you are now reaching the end of this acknowledgments and becoming mad at me for not including you then I hope you understand that, in service of brevity and finite page space, I was unable to include every member of the vast multitude to whom I am indebted. If you feel that you belong here then I'm sure you do and would love it if you were to write yourself in to your copy of this section.

Finally, thanks to you, the reader for picking up this work. I hope you find it valuable.

List of Figures

1.1	Complex Spin Structures	4
2.1	Types of Magnetism	9
2.2	Domains and Hysteresis Schematics	10
2.3	Basic Scattering Interaction	14
2.4	Example of PASANS Cross Sections	17
2.5	Scattering Geometry	19
2.6	Previous Results - Fe ₃ O ₄	21
2.7	Previous Results - CoFe ₂ O ₄	22
2.8	Spinel Structure	24
3.1	Low Resolution TEM	27
3.2	SAXS Characterization	27
3.3	High Resolution TEM & EELS	28
3.4	Hysteresis Loop	29
3.5	Blocking Temperature	29
3.6	NG7 Beamline	30
3.7	Experimental Geometry and ³ He Cell	31
3.8	Supermirror	32
3.9	Sector and Annular Averages	36
3.10	dDU vs Q	38
3.11	DU vs UD Differences	39
3.12	Data Splicing	41

LIST OF FIGURES

4.1	$ N ^2$	43
4.2	Comparing $ X_1 ^2$ to $ X_2 ^2$	44
4.3	$ X_2 ^2$ vs Temp and Field	45
4.4	$ Z ^2$ vs Temp and Field	46
4.5	Ratio vs Temp and Field	47
4.6	Coherent vs Incoherent Canting	49
4.7	HCP Model Layer and Particle	50
4.8	HCP Model Layers and Rotations	51
4.9	Model at 0.05 T, 400 K	54
4.10	Model at 0.2 T, 400 K	55
4.11	Model at 1.4 T, 200 K	56
5.1	vSANS range	58
5.2	Nanocubes	59
A.1	OC Macros	61

Contents

1	Introduction to Magnetic Nanoparticles	1
1.1	Uses	1
1.2	Magnetic Structure Determination	3
1.2.1	Traditional Magnetometry	4
1.2.2	Spectroscopy Methods	5
1.2.3	Scattering Methods	6
1.3	Thesis Organization	7
2	Background and Theory	8
2.1	Overview of Magnetism	8
2.2	Magnetism in Nanoparticles	9
2.2.1	Energy Considerations	10
2.2.2	Domains and Superparamagnetism	12
2.3	Neutron Scattering Theory	13
2.3.1	Small Angle Neutron Scattering (SANS)	13
2.3.2	Polarization Analyzed Small Angle Neutron Scattering (PASANS)	16
2.4	Previous Work	20
2.4.1	Fe_3O_4	20
2.4.2	CoFe_2O_4	21
2.5	Manganese Ferrite	22
2.5.1	Exchange interaction	22

CONTENTS

2.5.2	Anisotropy	23
2.5.3	Occupancy	23
3	Experimental Procedures	25
3.1	Sample Preparation	25
3.2	Characterization	26
3.3	Neutron Scattering	28
3.4	Polarized Neutron Scattering	30
3.4.1	Supermirror	30
3.4.2	Flipper	31
3.4.3	^3He Analyzer	32
3.5	Sample Conditions	33
3.6	Data Treatment	33
3.6.1	Determining Peak Polarization Values	38
3.6.2	Data recombination	40
4	Results	42
4.1	Structural $ \text{N} ^2$ Scattering	42
4.2	Magnetic $ \text{X} ^2$ Scattering	44
4.3	Magnetic $ \text{Z} ^2$, $ \text{YZ} ^2$ Scattering and $\frac{ \text{YZ} ^2}{ \text{Z} ^2}$	45
4.4	Model and Model Results	48
4.4.1	Model Explanation	49
4.4.2	Model Results	52
5	Summary and Future Work	57
5.1	Summary	57
5.2	Ongoing and Future Work	58
A	Custom IGOR Pro Analysis Macros	60

Chapter 1

Introduction to Magnetic Nanoparticles

Magnetic nanoparticles have diameters of about 5-500 nm and exhibit magnetic properties. They are the focus of much current research [1][2], with their small size and large surface to volume ratio leading to behaviors that can differ dramatically from the properties of a chemically identical substance in bulk. In addition, parameters like magnetic moment value, coercivity, and response to an applied field can be modified by their neighboring particles. These differences lead to interesting applications, but also new challenges in characterization, which has motivated this thesis on manganese ferrite nanoparticles.

1.1 Uses

Nanomagnets combine high specific surface area (small particles) and ease of separation (directed movement of the particles in liquids), properties that have led to applications in fields ranging from data storage, to water decontamination, to a variety of biomedical applications.

For computer applications, a binary value of 0 or 1 can be defined based

1.1. USES

on the direction of the net magnetization of a nanoparticle. This could allow for very compact data storage by reducing the size of a bit from the current technologies [3]. Magnetic nanoparticles, such as MnFe_2O_4 , have also found usage as a tool for removing heavy metals from contaminated water, combining the advantages of high specific surface area with ease of separation using directed movement via magnetic fields [4]. While there are many chelating agents such as EDTA that bind to heavy metals such as cadmium and lead, they can difficult to precipitate out of solution, thus removing the contamination. By binding such agents to magnetic nanoparticles with tailored magnetic properties, these chemicals could be deployed and then a magnetic field could be used to rapidly remove the unwanted metals to a very low concentration. Magnetic nanoparticles are also used to make smart fluids [5] [6], such as ferrofluids controlled with a magnet to form a seal around moving parts. As a liquid these seals would have very low friction resulting in a long lasting seal. Biomedical uses of magnetic nanoparticles have already been developed and many more are under consideration. One such use is for targeted drug delivery in which particles are attached to a drug, and are directed through the body with magnetic fields [7][8]. Nanoparticles of Fe_3O_4 have also been investigated for their ability to increase contrast in magnetic resonance imaging (MRI) [9] as the effects of superparamagnetism (See Section 2.2) can have an even greater contrast enhancing property than typically used paramagnetic materials. Hyperthermia is a further application of magnetic nanoparticles in which the nanoparticles are delivered to a tumor via attachment to specific antibodies, and a rapidly varying magnetic field is applied. Under these conditions, the nanoparticles will lose energy as heat, destroying the cells in their local environment, which allows for targeted destruction of cancerous cells [8].

The commonality of these applications is their reliance on nanoparticles with well-characterized magnetic properties. While physical properties such as size distribution are very important, magnetism presents unique character-

ization challenges as the behavior of individual nanoparticles must be studied in addition to how collections of nanoparticles interact with each other. In ferrofluids these interactions are particularly important as the response of dense collections determines the macroscale properties such as viscosity changes. For data storage if a single particle becomes superparamagnetic (Section 2.2) thermal fluctuations will cause bits to flip spontaneously, losing the stored data. Another possible complication is that dense collections of particles could influence each other, this might help retain information, but if the interaction is too strong, then it could become difficult to write the data. In biomedicine the interparticle interactions arising from clumps of particles will have a strong effect on outcomes of the procedure. Thus all these applications require a strong understanding of the inter and intrananoparticle magnetic properties.

1.2 Magnetic Structure Determination

While it is tempting to assume that under an applied magnetic field, nanoparticle spins will align and point uniformly, multiple theoretical investigations [10] [11] have found that the spin configurations within a nanoparticle can be far more complex. In Figure 1.1 there are examples of potential arrangements of spins within a nanoparticle. The various configurations were determined computationally for a variety of systems in which different energy terms were varied in their impact. Given the many potential applications, much study has been devoted to experimentally determining the magnetism; unfortunately many methods useful for bulk magnetometry are not particularly useful for the study of nanoparticles as they average out over the length scales of relevance. Here we will review a variety of standard methods and establish the potential of using the technique of polarization analyzed small angle neutron scattering (PASANS).

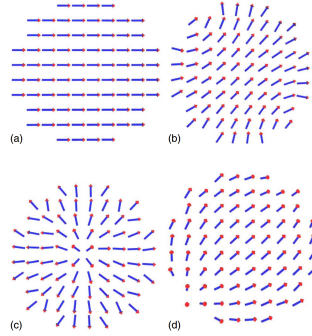


Figure 1.1: Demonstration of possible nanoparticle spin structures. The variation in structure is derived from variation in the strength of the surface anisotropy (to be discussed in Section 2.2). (a) Collinear ferromagnetic configuration with surface anisotropy = 0. (b) throttled configuration with surface anisotropy = 500. (c) hedgehog configuration, surface anisotropy = 2000. (d) artichoke configuration, surface anisotropy = -1500. Image taken from [10].

1.2.1 Traditional Magnetometry

Vibrating sample magnetometers (VSM), and super conducting quantum interference devices (SQUIDs), are the most often used methods to get moment (M) vs applied field (H) curves, and to investigate sample moment as a function of temperature. A vibrating sample magnetometer measures moment by vibrating a sample in a magnetic field and detecting the induced moment with pickup coils. While highly convenient for measuring the bulk moments of samples, it only reveals the magnitude of the average moment of the sample and so is less useful for probing individual nanoparticle moments. Another traditional magnetometry tool involves a superconducting quantum interference device (SQUID). The SQUID sensor relies on two Josephson junctions to measure extremely small currents induced by the Faraday effect in the magnetometer's pickup coils. However, the length scale of the detectable magnetic structure is inherently tied to limitations with the construction of small Josephson junctions. Standard SQUID devices measure the net mo-

ment of a whole sample, although, advances over the last fifty years have led to the development of μ SQUID which has a spatial resolution of less than a micrometer [13]. More recently work is being put into the development of nanoSQUIDs such as the carbon nanotube device described in [14]. Magnetic force microscopy is another nanoscale measurement technique in which a small probe sensitive to changes in magnetic flux is rastered across the sample allowing for high resolution determination of magnetic moments [15]. Along with magnetic force microscopy, μ SQUID and nanoSQUIDs are advanced nanoscale techniques that can measure individual nanoparticle magnetism. They are limited however, to the measurement of isolated particles, which is a major drawback as we are most often interested in how nanoparticles behave in a collection.

1.2.2 Spectroscopy Methods

Nuclear magnetic resonance spectroscopy (NMR) measures the resonance and decay behavior of nuclear spins, something that is highly dependent on their local magnetic environment. While it is frequently applied for the identification and characterization of organic molecules, it can also be applied to systems containing nuclei with nonzero spin. This range of uses extends to nanoparticles as demonstrated in [16]. In fact NMR can often provide data that is complementary to neutron scattering [17], which will be discussed in detail in Section 2.3.1.

Another spectroscopy method that has seen great use for spin determinations of magnetism is Mössbauer spectroscopy. The characteristics of absorption and emission of gamma radiation by nuclei in a sample is affected by the local magnetic environment and so is particularly useful for Fe^{+2} , and Fe^{+3} . It can be used to reveal fairly detailed information about nanoparticle magnetism [18]. The necessity of gamma radiation source, however increases the experimental difficulty. Furthermore both Mössbauer spectroscopy and NMR are sensitive only to nuclei with odd atomic numbers, meaning that

they sense ^{57}Fe but not the more common ^{56}Fe requiring doping of the sample or reliance on the small natural abundance of appropriate isotopes. Beyond this, both techniques give information about localized magnetism but do not reveal a great deal about the long range structure of the systems. Given that many of the potential applications such as hyperthermia can require fairly dense nanoparticle assemblies, internanoparticle interactions are of interest but NMR and Mössbauer fall short in their abilities to elucidate this.

1.2.3 Scattering Methods

Scattering methods are non-destructive and allow for the study of long range structure, while still being sensitive to the nanoscale [19]. Using scattering techniques to probe the length scales we are interested in requires small angle scattering, so the scattering methods we will consider are small angle X-Ray scattering (SAXS) and small angle neutron scattering (SANS).

These two methods are differentiable in what the source of scattering is. For X-Rays the scattering source is the electron cloud of the atoms so SAXS can be very useful for detecting positional information but is not sensitive to magnetic moments of the sample. Neutrons have magnetic moments and so interact with both the nuclei and magnetic moments of a sample. Thus they can, like X-Rays, be used to determine the structure of a sample, but are simultaneously capable of investigating both the magnetic ordering, and small scale structure.

In recent years there have been new developments employing polarized neutrons to probe the magnetic signature of particles [20][21][22]. Polarization analyzed small angle neutron scattering (PASANS) is a specific type of SANS that allows for the complete separation of the magnetic and nuclear components of scattering with much greater ease than in pure SANS. PASANS is sensitive to both local order and long range ordering of the sample and so is an ideal tool for investigation of nanomagnetism.

1.3 Thesis Organization

In the past decade exciting new avenues for the study of magnetic nanoparticles have been opened up by the development of Polarized SANS. This thesis will focus on the application of PASANS scattering to manganese ferrite nanoparticles and is organized as follows: Chapter 2 reviews the relevant physics of magnetism in nanoparticles, the theory of SANS and PASANS, previous work by Prof. Ijiri, collaborators and former students, and the justifications for studying manganese ferrite in particular. Chapter 3 describes experimental procedures including sample preparation, characterization, data collection, and how the data was treated. Chapter 4 presents the current state of our understanding of the magnetic structure of manganese ferrite nanoparticles and presents a model that shows promise for capturing the observed behavior. Chapter 5 summarizes the results and presents directions for future work. The appendix contains code that was written for this project that aids greatly in the analysis of PASANS data.

Chapter 2

Background and Theory

2.1 Overview of Magnetism

This section follows the discussion by Hasz [23]. There are four types of magnetism that appear in bulk materials that are also of relevance to a discussion of nanomagnetism: ferromagnetism, antiferromagnetism, ferrimagnetism, and paramagnetism. All are the result of a net spin resulting from electrons giving rise to a magnetic moment. Paramagnetism is the alignment of moments due to an external magnetic field and does not involve interactions between the spins. This tends to be a weak effect and alignment will disappear upon removal of the external field. In contrast, ferromagnetism consists of spins naturally aligning due their interaction via some exchange mechanism. As can be seen in Figure 2.1, in a ferromagnet the spins interact and tend to align resulting in a permanent magnetic moment. Iron, cobalt, nickel, and gadolinium all exhibit natural ferromagnetism. Antiferromagnetism is also a ground state ordering of spins, however the spins tend to antialign resulting in a net zero moment, this is also demonstrated in Figure 2.1. The final image in Figure 2.1 is of ferrimagnetism, in which, the spins tend to anti-align but not such that the magnetic moment sums to zero. The net magnetic moments tend to form domains of aligned particles as demon-

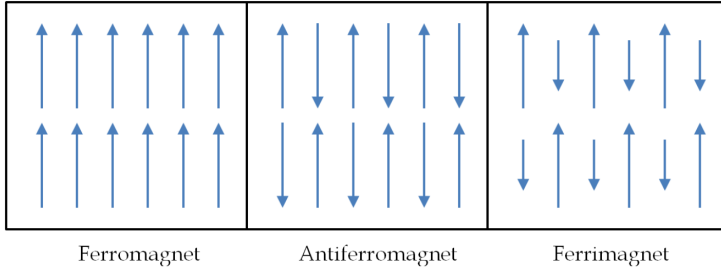


Figure 2.1: Ferromagnets have a net moment due to the energetically favorable alignment of spins. Antiferromagnets have no net moments due to the tendency of spins to anti-align with their neighboring spins. Ferrimagnets share the same alignment scheme as antiferromagnets but have a net moment as the spins do not completely cancel out. Taken from [23].

strated in Figure 2.2a, regions that can grow, shrink, or rotate depending on the applied magnetic field and other parameters.

In this thesis we will primarily be concerned with ferro- and ferrimagnetic systems, which are often described in terms of a hysteresis loop. A cartoon of a hysteresis loop can be seen in Figure 2.2b demonstrating that once the magnetization of a sample has been aligned to one direction it requires a field applied opposite the magnetization to return the magnetization to zero. The width of the loop can be described by the coercivity H_C , a greater value of which corresponds to more difficulty in flipping the magnetization direction. The magnetization value at which an increase in applied field does not result in an increase in magnetization is known as the saturation magnetization M_S , and the remanent magnetization magnetization, M_R , is the magnetization after applied field is removed.

2.2 Magnetism in Nanoparticles

The magnetic behavior exhibited by nanoparticles can differ significantly from the magnetic behavior of the same material in bulk. The high surface to volume ratio and other effects stemming from the small size of nanoparti-

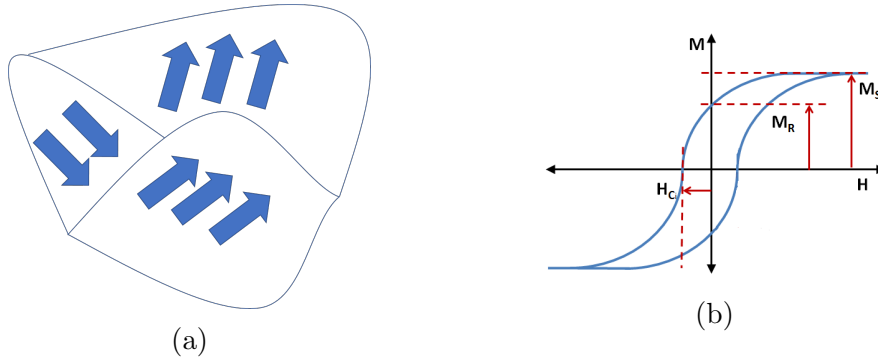


Figure 2.2: (a) Illustration of domains in a ferromagnet.(b) A schematic hysteresis loop of moment (M) vs applied magnetic field (H). This image illustrates the saturation magnetization M_s , remanent magnetization M_R and the intrinsic coercivity H_{Ci} . Taken from [24].

cles can transform the energy landscape of a material leading to interesting differences between nano and bulk magnetism. Here we will discuss the primary energy terms that need to be considered following the discussion by Booth [24], Hasz [23], and Majetich [25].

2.2.1 Energy Considerations

There are four energy terms that need to be considered when studying a system of interacting nanoparticles [23].

Zeeman

In the presence of a magnetic field \vec{H} a magnetic dipole \mathbf{m} will have an energy associated with its orientation relative to \vec{H} of [26],

$$U = -\mathbf{m} \cdot \vec{H}. \quad (2.1)$$

This energy is also referred to as the Zeeman energy and can prove to be an important contributor in energy models of magnetism in nanoparticles under

applied field [27].

Magnetocrystalline Anisotropy

The internal energy of a magnetic crystal can depend on the direction of the magnetization. As a result of crystalline symmetry, there may be one or more axes, known as easy axes, onto which it is energetically favorable for spins to align [28]. Many substances, such as the materials considered in this work, have a cubic anisotropy, which can be taken at first approximation to be uniaxial with the anisotropy energy density described as $E_A = K \sin^2(\phi)$ where ϕ is the angle between the internal magnetization and the easy axis and, K is the anisotropy constant [29].

At the surface of nanoparticles the crystal stucture symmetry is broken which can create preferred directions, giving rise to what is known as surface anisotropy. This can also play a role in determining nanoparticle magnetism as nanoparticles have a high surface to volume ratio.

Exchange

Magnetic moments in the same crystal lattice can have an interaction known as the Heisenberg Exchange Interaction or simply the exchange interaction [30]. Two spins can interact electrostatically through overlapping charge distributions, this interaction along with the Pauli Exclusion principle leads to an energy of

$$U_{\text{exch}} = -J_{\text{exch}} \mathbf{S}_1 \cdot \mathbf{S}_2, \quad (2.2)$$

where J_{exch} is known as the exchange integral of constant and \mathbf{S}_1 and \mathbf{S}_2 are the two interacting spins. J_{exch} can be positive or negative depending on the specifics of the material under consideration. In general J_{exch} will scale linearly with the Curie temperature of the material [31].

Dipole

Generically the strength of the dipole interaction is [30],

$$U_{\text{dipole}} = \frac{\mu_0[\mathbf{m}_1] \cdot \mathbf{m}_2 - 3(\mathbf{m}_1 \cdot \hat{\mathbf{r}})(\mathbf{m}_2 \cdot \hat{\mathbf{r}})}{4\pi r^3}, \quad (2.3)$$

with $\mathbf{r} = \mathbf{r}_1 - \mathbf{r}_2$ as the vector between magnetic dipoles \mathbf{m}_1 and \mathbf{m}_2 , and μ_0 the Bohr magneton. In the context of nanoparticle magnetism the dipole energy refers to the interparticle interactions of magnetic moments. Typically the associated energy is smaller than the exchange and anisotropy energies for neighboring moments, but in a collection, the overall interaction, summed over multiple nanoparticles can be significant.

2.2.2 Domains and Superparamagnetism

In bulk, materials often form multiple domains whose magnetization directions vary in order to minimize energy and close flux lines inside the sample. In contrast, magnetic nanoparticles are often small enough that they become monodomain. The maximum diameter to have a monodomain particle can be written as [25]

$$d_{cr} = \pi S \sqrt{\frac{J}{K \cdot a}}, \quad (2.4)$$

where S is the spin per atom, J is the exchange constant, K is the uniaxial anisotropy energy constant, and a is the lattice constant defining the physical dimensions of the intra-particle crystal lattice.

In monodomain particles, the individual magnetic moments behave as a single moment for the entire particle. In such a situation the spins must coherently rotate direction in order to change the particles magnetization which gives rise to a non-zero H_c . However, at certain size and temperature combinations the coercivity can drop to zero and the particles are said to be superparamagnetic. This occurs when the magnitude of thermal energy

2.3. NEUTRON SCATTERING THEORY

fluctuations $k_b T$ is comparable to the anisotropy energy KV . In zero applied field with a uniaxial anisotropy there are two equilibrium orientations for the magnetization, one of which will become preferential when a magnetic field is applied. The particle magnetization needs to rotate through a higher energy configuration in order to reach the preferred axis. The attempt frequency for this occurring is on the order of the Larmor precession frequency, giving a time scale of $\tau_0 10^{-9}$. The time to equilibration will then be

$$\tau = \tau_0 e^{KV/k_b T}. \quad (2.5)$$

If the time for a measurement of the magnetization, τ_m , is larger than τ then the particles will all equilibrate before the end of the measurement and a hysteresis measurement will result in a coercivity of 0, this is the condition of superparamagnetism. If T is large enough then we will have $\tau_m < \tau$, so superparamagnetism is function of temperature. With a known τ_m we can find the temperature at which the particle transitions superparamagnetism as

$$T_B = \ln\left(\frac{\tau_m}{\tau_0}\right) KV, \quad (2.6)$$

which is known as the blocking temperature. Experimentally, this is the lowest temperature for which $H_c = 0$, or the temperature at which a zero field cooled and field cooled magnetization vs temperature curve meet.

2.3 Neutron Scattering Theory

2.3.1 Small Angle Neutron Scattering (SANS)

The fundamental event in a scattering experiment is the interaction of a neutron with a scattering center resulting in a change of momentum for the neutron, as illustrated in Figure 2.3. With \mathbf{k}_i as the wavevector of the incident neutron and \mathbf{k}_f as the outgoing wavevector, it is useful to define \mathbf{Q}

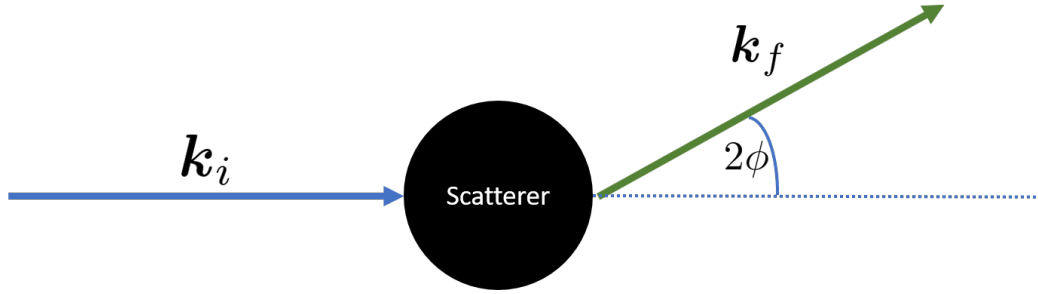


Figure 2.3: Illustration of the basic action in scattering, with \mathbf{k}_i as the initial wavevector, \mathbf{k}_f the final wavevector, and 2ϕ the angle between.

the scattering vector as

$$\mathbf{Q} = \mathbf{k}_f - \mathbf{k}_i. \quad (2.7)$$

In the work of this thesis, all scattering was elastic such that $|\mathbf{k}_i| = |\mathbf{k}_f| = \frac{2\pi}{\lambda}$. With this fact and the use of the angle 2ϕ in Figure 2.3, we find the magnitude of \mathbf{Q} is

$$|\mathbf{Q}| = Q = \frac{4\pi \sin(\phi)}{\lambda}. \quad (2.8)$$

If we combine this with Bragg's Law $N\lambda = 2d \sin(\phi)$, we find that $Q = \frac{4\pi \sin(\phi)}{\lambda} = \frac{2\pi N}{d}$ which in the case of $N = 1$ reduces to

$$|\mathbf{Q}| = Q = \frac{2\pi}{d}, \quad (2.9)$$

where d is the characteristic length scale of crystalline planes or other features. With Nanoparticles with a radius of approximately 30 Å we are primarily interested in length scales of 50-5000 Å. Consequently the values of Q of interest range from $.001 \text{ \AA}^{-1}$ for long range correlations to 2 \AA^{-1} for short range correlations.

Since we are not interested in scattering off single atoms or single nanoparticles, we need to consider the effects of having multiple scattering centers. In a generic scattering experiment the waves scattered off different scattering centers will interfere either constructively or destructively at the detector

2.3. NEUTRON SCATTERING THEORY

resulting in an intensity of

$$I \propto \left| \sum_K \rho(K, \mathbf{Q}) e^{i\mathbf{Q} \cdot \mathbf{R}_K} \right|^2, \quad (2.10)$$

where $\rho(K, Q)$ describes the scattering length density (SLD) for the Kth scatterer which gives the effect of scattering, and \mathbf{R}_K is the position of this scatterer. For the scattering of neutrons off a nucleus, the values f_K are isotope-specific and do not vary in a simple way with atomic number. Neutrons are thus a powerful tool for determining structure through their ability to distinguish between isotopes as well their ability to pick lighter elements such as hydrogen [32].

However, the true power of neutrons for studies of magnetic materials is derived from their intrinsic magnetic moment of $-1.912 \mu_N$ where $\mu_N = \frac{e\hbar}{2m_p}$ is the nuclear magneton. Neutrons thus interact with both the nuclei and the outer orbitals that give rise to the magnetic moment of an atom. With two separate scattering processes, the amplitude of the scattered wave will now include both nuclear and magnetic scattering. The nuclear $|N|^2$ and magnetic $M_{x,y, \text{ or } z}$ amplitudes are defined as

$$N, M_{x,y,z}(\mathbf{Q}) = \sum_K \rho_{N,M_{x,y, \text{ or } z}}(K, \mathbf{Q}) e^{i\mathbf{Q} \cdot \mathbf{R}_K}. \quad (2.11)$$

where $\rho_{N,M_{x,y, \text{ or } z}}(K, \mathbf{Q})$ is the Nuclear or magnetic scattering length density for the K^{th} scatterer, and \mathbf{R}_K is the location of the K^{th} scatterer relative to the origin. The final intensity of scattering will be the squared sum of the nuclear and magnetic Fourier transform components defined in Eq. 2.11. However, the case of magnetic scattering is slightly more complicated than nuclear as only the component of a magnetic moment that is perpendicular to \mathbf{Q} can participate in scattering. This fact is embodied by what is known

2.3. NEUTRON SCATTERING THEORY

as the Halpern-Johnson vector [33]

$$\Upsilon(\mathbf{Q}) = |\mathbf{M}|[\hat{\mathbf{M}} - (\hat{\mathbf{Q}} \cdot \hat{\mathbf{M}})\hat{\mathbf{Q}}], \quad (2.12)$$

which is used in the calculation of scattering below.

2.3.2 Polarization Analyzed Small Angle Neutron Scattering (PASANS)

While SANS is powerful for its dependence on magnetic as well as structural scattering, it can be difficult to separate the magnetic and nuclear components of the scattering without probing the polarization of the neutrons. As developed by Moon [34], the theory of scattering with polarized neutrons allows for a cleaner separation of the magnetic and nuclear components of the scattering. In polarization analyzed small angle neutron scattering (PASANS) the incoming neutron beam is polarized with neutrons in beam polarized to be entirely spin up or spin down when they reach the sample. After scattering off the sample, the neutron spins will either stay the same or flip and the spin direction of the scattered neutrons is sensed resulting in four scattering cross-sections: $\sigma^{\uparrow\uparrow}$, $\sigma^{\downarrow\downarrow}$, $\sigma^{\downarrow\uparrow}$, $\sigma^{\uparrow\downarrow}$ (also referred to as UU, DD, DU, and UD). Examples of such cross sections are shown in Figure 2.4, which are the recorded intensities on a 2-D detector some distance from the sample.

Of the four different scattering data sets there are two distinct subsets: Non spin flip (NSF) scattering, UU and DD, in which the neutron spin did not change on scattering off the sample, and spin flip (SF) scattering, DU and UD, in which the scattered neutron has opposite spin of the incident neutron. The power of PASANS is derived from the fact that coherent nuclear scattering does not cause neutrons to flip their spins, so the information contained in the SF cross sections will reflect purely magnetic scattering¹.

¹There will also be incoherent nuclear scattering in the SF, but we will take it as negligible.

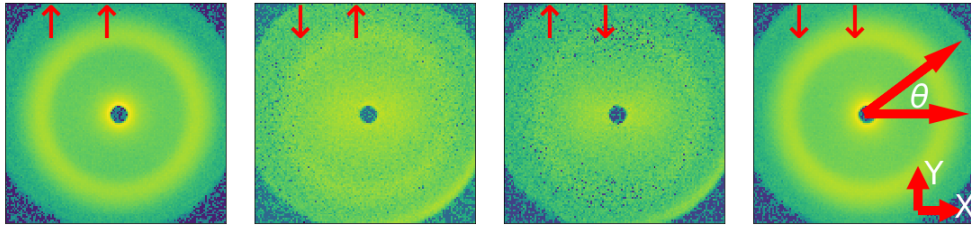


Figure 2.4: The 2D PASANS data after the polarization correction described in greater detail in Section 3.6. Each point corresponds to one pixel of the detector and distance from the center gives \mathbf{Q} . The angle θ is used for calculating the 1D Fourier transforms of different components of magnetization below. Data are the result of scattering from a sample of manganese ferrite at 0.3 T and 400 K.

Taking N as the structural scattering amplitude we can use the Halpern-Johnson vector, Eq. 2.12, to calculate the crosssections as [33],

$$\sigma^{\uparrow\uparrow}, \sigma^{\downarrow\downarrow} = \frac{1}{2}|N \pm \Upsilon_X|^2, \quad (2.13)$$

$$\sigma^{\uparrow\downarrow}, \sigma^{\downarrow\uparrow} = \frac{1}{2}| - \Upsilon_Y \mp \Upsilon_Z|^2, \quad (2.14)$$

demonstrating the dependence of the SF scattering purely on the portion of the sample's magnetic moment that is perpendicular to \mathbf{Q} .

As the technology to create polarizers capable of capturing a large 2D cross section has developed [35][36][37], studies have been conducted on the application of polarized neutrons to small angle scattering which as developed by Krycka et. al [38][33] allows for the determination of Fourier transforms of the Cartesian components of the moments of the sample.

We can define useful quantities $\mathbb{A}, \mathbb{B}, \mathbb{C}$ as various combinations of scattering cross sections as in Table 2.1, with \mathbb{A} being the sum of the NSF cross-sections, \mathbb{B} the difference, and \mathbb{C} the sum of the SF.

Using the geometry in Figure 2.5, we can also define $\mathbb{A}, \mathbb{B}, \mathbb{C}$ in terms of the Fourier transforms of the nuclear and magnetic components as follows

2.3. NEUTRON SCATTERING THEORY

\mathbb{A}	$\sigma^{\uparrow\uparrow} + \sigma^{\downarrow\downarrow}$
\mathbb{B}	$\sigma^{\downarrow\downarrow} - \sigma^{\uparrow\uparrow}$
\mathbb{C}	$\sigma^{\uparrow\downarrow} + \sigma^{\downarrow\uparrow}$

Table 2.1: Definition of the combinations of 2D data used to calculate the 1D Fourier transforms below.

[33]:

$$\begin{aligned}\mathbb{A}(\mathbf{Q}) = & |N(|\mathbf{Q}|, \theta)|^2 + |\mathbf{M}_x|^2 \sin^4(\theta) + |\mathbf{M}_y|^2 \cos^2(\theta) \sin^2(\theta) \\ & - 2|\mathbf{M}_x||\mathbf{M}_y| \overline{\cos}(\varphi_{M_x} - \varphi_{M_y}) \sin^3(\theta) \cos(\theta)\end{aligned}\quad (2.15)$$

$$\mathbb{B}(\mathbf{Q}) = |N(|\mathbf{Q}|, \theta)|^2 + |\mathbf{M}_x|^2 \sin^4(\theta) + |\mathbf{M}_y|^2 \cos^2(\theta) \sin^2(\theta) \quad (2.16)$$

$$\begin{aligned}\mathbb{C}(\mathbf{Q}) = & |\mathbf{M}_z(|\mathbf{Q}|, \theta)|^2 + |\mathbf{M}_y(|\mathbf{Q}|, \theta)|^2 \cos^4(\theta) + |\mathbf{M}_x(|\mathbf{Q}|, \theta)|^2 \cos^2(\theta) \sin^2(\theta) \\ & \times \overline{\cos}(\varphi_{M_x} - \varphi_{M_y}) \sin(\theta) \cos^3(\theta),\end{aligned}\quad (2.17)$$

where we have explicitly put in that the polarization axis of the neutron is perpendicular to its propagation direction. The $\overline{\sin}$ and $\overline{\cos}$ terms are averaged over the sample and contain φ terms that represent the phase of various components of scattering. If $\overline{\cos}(\varphi_\alpha - \varphi_\beta) = \pm 1$ or 0 then α and β are said to be in-phase and out-of-phase respectively. At angles of $\theta = 90^\circ$ and 0° , these equations simplify allowing us to extract the structural $|N|^2$

$$|N|^2 = |N(|Q|, 0^\circ)|^2 = \mathbb{A}(|Q|, 0^\circ), \quad (2.18)$$

the total $|\mathbf{M}_X|^2$ as,

2.3. NEUTRON SCATTERING THEORY

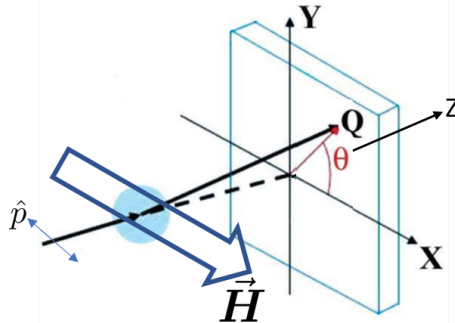


Figure 2.5: Basic geometry to be used for the theory of scattering going forward. The neutron polarization, \hat{p} is perpendicular to the propagation direction which is along the Z axis, and parallel to the applied field \vec{H} which is parallel to the X axis. \mathbf{Q} has been depicted on the detector (large slab) and θ is defined as the angle between \mathbf{Q} and the X axis. Adapted from [33].

$$|X_1|^2 = |M_x(Q)|^2 = \mathbb{A}(|Q|, 90^\circ) - \mathbb{A}(|Q|, 0^\circ), \quad (2.19)$$

the $|M_X|^2$ that is coherent (in phase) with the nuclear scattering as,

$$|X_2|^2 = |M_x(Q)|^2 = \mathbb{B}^2(Q)/(4 \sin^4(\theta) \cdot \mathbb{A}(|Q|, 0^\circ)), \quad (2.20)$$

$|M_Z(|Q|, 90^\circ)|^2$ as,

$$|Z|^2 = |M_z(Q)|^2 = \mathbb{C}(|Q|, 90^\circ), \quad (2.21)$$

and, the sum $|M_Y(|Q|, 0^\circ)|^2 + |M_Z(|Q|, 0^\circ)|^2$ as,

$$|YZ|^2 = |M_y(Q)|^2 + |M_z(Q)|^2 = \mathbb{C}(|Q|, 0^\circ). \quad (2.22)$$

2.4 Previous Work

2.4.1 Fe₃O₄

Previous work by Professor Ijiri, earlier students, and collaborators investigated mono-disperse Fe₃O₄ nanoparticles via PASANS. Early work focused on developing the technique of PASANS in order to separate the magnetic and structural scattering making magnetite, one of the most studied nanoparticles, a natural first system. Those advances allowed for the discovery of a highly temperature dependent variation in the long-range interparticle magnetic correlations at remanence [39]. Later work examined the results of polarized neutron scattering over a range of applied magnetic fields and temperatures [40]. In Figure 2.6a we can see the Fourier Transform components of the scattering derived from Eqs. 2.18, 2.19, 2.20 and, 2.21 for Fe₃O₄ particles at 200 K under with $\vec{H} = 1.2$ T applied along the X axis. For that data $|M_x|^2$ has a peak that is highly correlated with the structural scattering peak which is to be expected given the strength of the applied field. In contrast, the $|M_z|^2$ scattering data have a dip instead of a peak. Analysis by Krycka *et al.* found that this dip corresponds to the form factor of a spherical shell with a component of magnetization along the Z axis, further analysis revealed canted shells at 160, 300, and 320 K, but no ordered shell when zero-field cooled to 10 K before application of the field [40].

Finally an energy-balance model of the nanoparticles based on the magnetocrystalline anisotropy, dipolar, exchange and Zeeman energies was developed to reproduce the evolution of shell thickness with temperature [41]. That model found that the shells spins in tetrahedral sites in the inverse spinel lattice were canted at an angle between 23° and 42° from the applied 1.2 T field. This shell was completely magnetic in origin, and could grow and shrink changes in applied field and temperature.

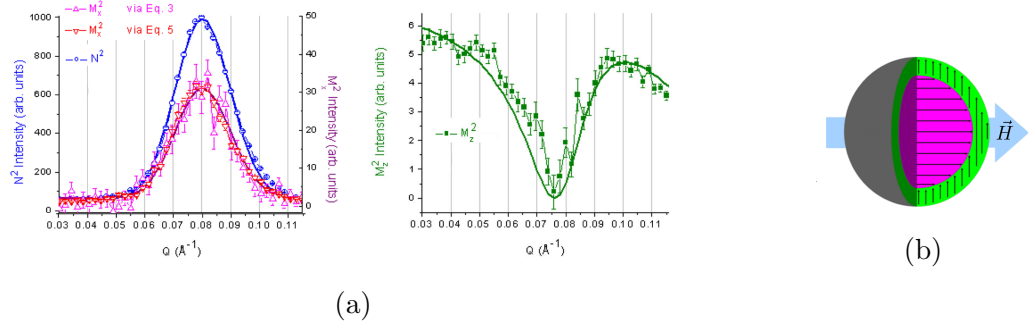


Figure 2.6: (a) PASANS data from Fe_3O_4 nanoparticles at 1.2 T, 200 K with the field applied along the X axis. Note the peak in $|M_x|^2$ that is correlated with the structural $|N|^2$ as well as the dip in $|M_z|^2$. (b) The core-shell model of the magnetization of the nanoparticles under an applied field \vec{H} developed on the basis of (a). Both Figures adapted from [40].

2.4.2 CoFe_2O_4

Following the studies of Fe_3O_4 nanoparticles work continued on CoFe_2O_4 nanoparticles to search for analogous magnetic structures and to test the generalizing potential of the energy model that had been developed for Fe_3O_4 [23]. The results of PASANS for these particles are reproduced here in Figure 2.7. As with Fe_3O_4 there is a Bragg peak in $|M_x|^2$ at the same length scale as the structural Bragg peak; the CoFe_2O_4 particles however, differ in the behavior of $|M_z|^2$. For these nanoparticles, there was no dip in $|M_z|^2$ implying that unlike the iron oxide particles, no magnetic shell develops under high applied field. Instead the scattering curves for both $|M_x|^2$ and $|M_z|^2$, shown in Figure 2.7, were found to correspond to spherical forms factors of the same radius implying that the magnetization was uniform throughout the nanoparticle. While uniform, the magnetization was not trivial as there were equal X and Y components of the moment, which lead to the interpretation of the moments throughout the particles canting off the X axis in moderate to high applied fields. Importantly the canting was not correlated between nanoparticles so the component of the moments off the X axis sums to zero

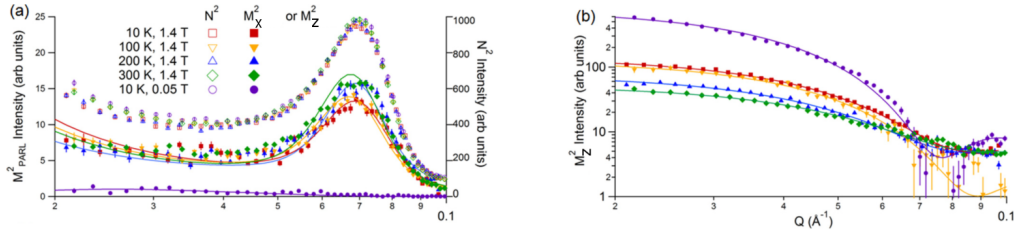


Figure 2.7: Results from a PASANS experiment studying CoFe_2O_4 nanoparticles with an applied magnetic field along the X axis. (a) Structural and $|M_x|^2$. (b) $|M_z|^2$. Adapted from [27]

macroscopically. The data were then used to develop an energy model based on Zeeman and anisotropy energies which found that both the tetrahedral and octahedral sites tilt at an angle that depends on both the temperature and applied field, predicting a tilt as large as 10° even in magnetic fields as large as 10 T [41]. These data explain the common observation of non-bulk magnetization through an uncorrelated canting.

2.5 Manganese Ferrite

Following the studies of Fe_3O_4 and CoFe_2O_4 a natural next step was to study manganese ferrite nanoparticles. Manganese has both important similarities and differences from both cobalt ferrite and iron oxide nanoparticles.

2.5.1 Exchange interaction

As previously mentioned the strength of the exchange interaction scales linearly with the curie temperature, so based on the value of T_C in Table 2.2 we expect manganese ferrite to have a much weaker exchange interaction than either cobalt ferrite or iron oxide.

Fe_3O_4	848 K
CoFe_2O_4	793 K
MnFe_2O_4	568 K

Table 2.2: Curie Temperatures for the ferrites of relevance to this thesis. Values from [31].

2.5.2 Anisotropy

A study by Rondinone et al. found CoFe_2O_4 nanoparticles with a mean diameter of 8.5 nm to have an anisotropy constant of .223 J/cm³ [42]. This is very large magnitude compared to the values at room temperature of -.002 J/cm³ and -.011 J/cm³ for MnFe_2O_4 and Fe_3O_4 respectively [28].

2.5.3 Occupancy

Beyond the differences in manganese ferrite from CoFe_2O_4 and Fe_3O_4 in terms of the exchange energy and its anisotropy curve, it is an interesting system with regards to the occupancy of sites in its crystal structure. Like ferrite and cobalt ferrite, the crystal structure of manganese ferrite belongs to the spinel group class of minerals, the crystal structure of which can be seen in Figure 2.8. Spinel structures can be further classified into classes of normal and inverse spinels. In normal spinel structures the divalent (2+) ions occupy the octahedral sites in the material while the trivalent (3+) occupy tetrahedral sites. Both the CoFe_2O_4 and Fe_3O_4 samples from previous work have inverse spinel structures [27][41]. In contrast to this, the occupancy of manganese ferrite is not as clear. Neutron diffraction studies have found that manganese ferrite has a nearly normal spinel structure with 81% of the tetrahedral sites occupied by Mn^{2+} [43].

Given the markedly different magnetic structures between CoFe_2O_4 and Fe_3O_4 nanoparticles, and the differences manganese ferrite has in both chemical structure and energy considerations, we can expect study of manganese ferrite nanoparticles reveal important new features in nanomagnetism.

2.5. MANGANESE FERRITE

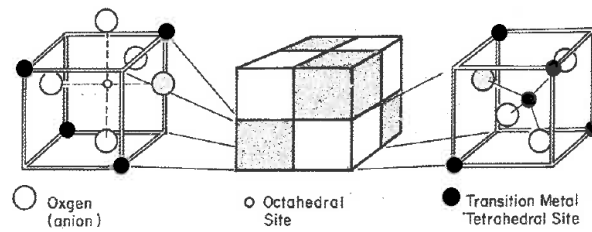


Figure 2.8: Illustration of the spinel structure. The shaded oxygen atom is shared between both cells. The inverse spinel structure discussed in the text simply reverses which metal ions occupy the tetrahedral and octahedral sites. Taken from [44].

Chapter 3

Experimental Procedures

3.1 Sample Preparation

The particles under consideration in this thesis were synthesized by Dr. Samuel Oberdick (PhD. '16) working under Dr. Sara Majetich at Carnegie Mellon University. They were made by mixing iron acetylacetone, and manganese acetylacetone in a 2:1 ratio, and decomposing in the presence of 1,2-hexadecanediol, oleic acid, and oleyamine based on the procedure outlined in Sun, *et al* [45]. This method resulted in a monodisperse manganese iron oxide particles suspended in a solution of toluene with a thin oleic acid coating on the particles.

In order to achieve a more controlled study of the magnetic interactions, an ordered arrangement of nanoparticles is more useful. To this end, the nanoparticles were crystallized by slowly diffusing a poorly coordinating solvent into a stable dispersion of manganese ferrite nanoparticles in toluene following the method of Talapin *et al.* [46].

3.2 Characterization

Both transmission electron microscopy (TEM), Figure 3.1, and small angle X-ray scattering, Figure 3.2, were used to characterize the size of the the nanoparticles. Dr. Oberdick performed the standard TEM to find the particles to be 7.5 ± 1 nm in diameter. This is consistent with the small angle X-ray scattering (SAXS) performed by Jason Heitler-Klevans at Oberlin College. Figure 3.2a shows the result of SAXS measurements on the particles suspended in toluene.

The data from a SAXS measurement of the particles in solution, Figure 3.2a, was used to find that the distribution of nanoparticle radii was described by a log normal distribution with $\sigma = 0.13$ and mean 37.4 Å. As shown in Figure 3.2b a SAXS pattern for the crystallized nanoparticles was also recorded. Keeping the value for nanoparticle radius from the in-solution scattering the crystallized data were fit to an FCC paracrystal model [47] and the lattice parameter was found to have a value of $113.19 \pm .07$ Å. The instrumentation used for the SAXS was a Rigaku Ultima IV 285m X-ray diffractometer (acquired through NSF grant DMR-0922588 at Oberlin College) in the small angle X-ray scattering (SAXS) configuration.

Further characterization work was performed by Dr. Demie Kepartsoglou and Dr. Vlado Lazarov with high resolution TEM at University of York. Figure 3.3a, shows that high resolution TEM demonstrating that the nanoparticles have a spinel structure throughout. They also performed electron energy loss spectroscopy (EELS), Figure 3.3b, leading to the surprising result that the nanoparticles are not chemically uniform. A result backed up by Mössbauer spectroscopy done by Johan von Lierop (Univ. of Manitoba) that was inconsistent with a stoichiometry of $MnFe_2O_4$. Rather, there is a core composed primarily of iron oxide and a manganese rich shell.

The bulk magnetic properties of the sample were probed using a Quantum Design Superconducting Quantum Interference Device (SQUID) magnetometer. Dr. Oberdick performed hysteresis measurements, Figure 3.4,

3.2. CHARACTERIZATION

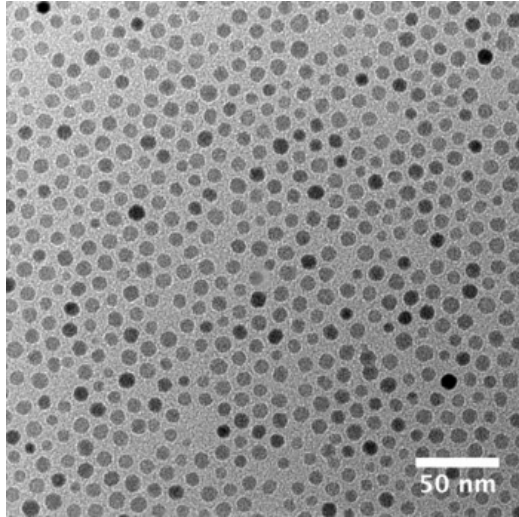


Figure 3.1: Transmission Electron Microscopy (TEM) image showing a particle diameter of 7.5 ± 1 nm. This TEM work was performed by Dr. Oberdick.

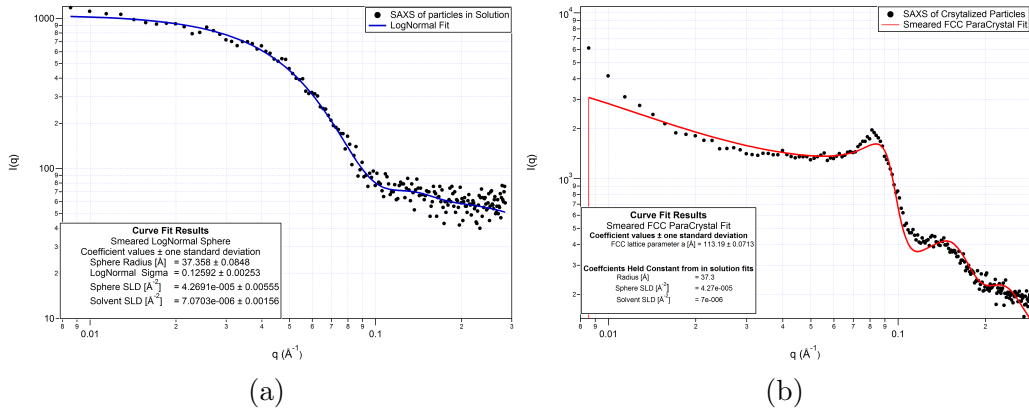


Figure 3.2: (a) SAXS data and fit based on a LogNormal distribution of sphere sizes of manganese ferrite nanoparticles in a solution of toluene (b) FCC paracrystal fit of SAXS data from the nanoparticles after crystallization. For the crystal fits several parameters were held constant on the basis of the in solution fits which still resulted in reasonable fits implying that these values are good to use. Data for both images are from work done by Jason Heitler-Klevans at Oberlin College.

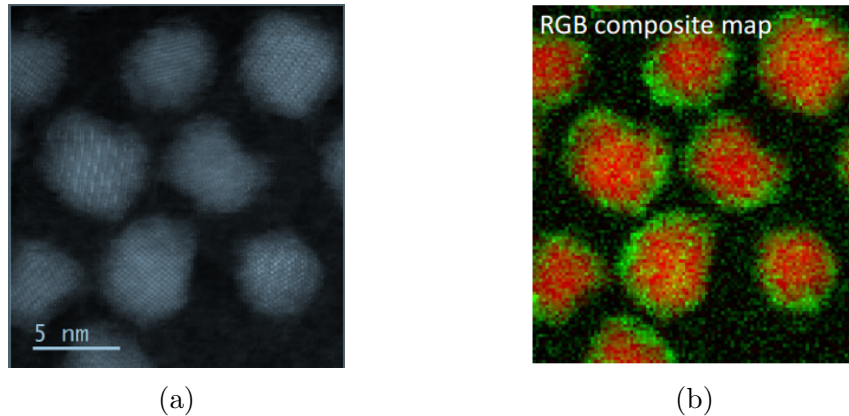


Figure 3.3: (a) High resolution transmission electron microscopy showing that the nanoparticles have a spinel structure throughout. (b) Map of the density of Mn (green) and Fe (red) in the nanoparticles derived from electron energy loss spectroscopy (EELS). Data for both figures are from Demie Kepartsoglu and Vlado Lazarov, University of York.

at temperatures of 10 K and 300 K with applied fields ranging in strength from -30 to 30 kOe (-3, 3 T). From this there was found to be a decrease in saturation magnetization with higher temperature which could correspond to a softening of the magnetic moments. Furthermore, at 10 K the hysteresis loop had an enclosed area while the enclosed area was zero at higher temperatures. This is consistent with the blocking temperature, Figure 3.5, of approximately 30 K.

3.3 Neutron Scattering

Neutron scattering experiments were performed on the NG7 30m SANS beamline at the National Institute of Standards and Technology Center for Neutron Research in Gaithersburg, Maryland. The geometry of the beamline, shown in Figure 3.6, gives access to a Q range of 0.8×10^{-3} to 0.7 \AA^{-1} . A mechanical velocity selector can be used to select the wavelength range of incident neutrons between 5 and 20 \AA , in this work a wavelength of 5.5 \AA

3.3. NEUTRON SCATTERING

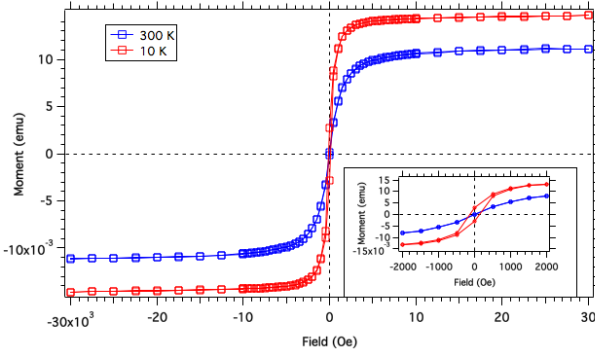


Figure 3.4: Hysteresis loop data at 10 and 300 K for the nanoparticles recorded by Dr. Oberdick. From the difference in saturation magnetization, we see a softening of the magnetic moment at higher temperature. From the inset we can see that at 300 K, which is above the blocking temperature, the hysteresis loop has no enclosed area so the nanoparticles are acting paramagnetically at that temperature.

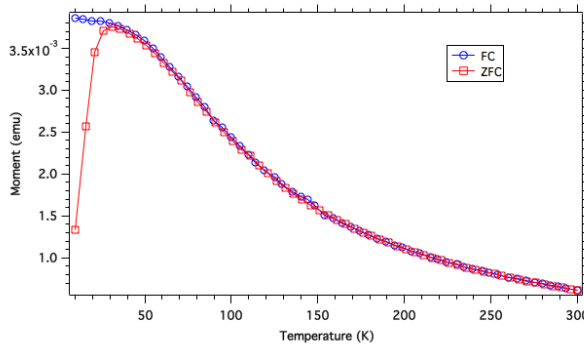


Figure 3.5: Comparison of the moment vs temperature for the nanoparticles when cooled under an applied field (FC) and cooled with zero applied field (ZFC). Analysis of this curve shows a blocking temperature of approximately 30 K. Data are from Dr. Oberdick.

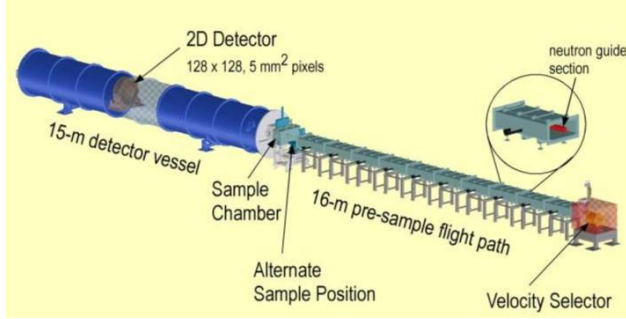


Figure 3.6: Diagram of the NG7 beamline. There is a maximum of 30 m from velocity selector to detector with the sample in middle. The movable 2D detector allows for the Q range of the instrument to be 0.8×10^{-3} to 0.7 \AA^{-1} . Image taken from [48].

was used, and the detector position was varied in order to probe Q values over an order of magnitude between 10^{-2} and 10^{-1} \AA^{-1} .

3.4 Polarized Neutron Scattering

The use of polarized neutrons further complicates the experimental setup by adding several of the components in Figure 3.7a in order to control the polarization of the neutrons both before and after scattering from the sample.

3.4.1 Supermirror

Coming out of the reactor source the neutron beam contains an equal number of spin up and spin down neutrons. In order to control the polarization of the neutrons scattering off the sample the beam is passed through a FeSi supermirror, which ideally completely polarizes the beam by retaining only spin up neutrons. As can be seen from the simplified schematic in Figure 3.8, it accomplishes this via the preferential reflection of one polarization from a multilayer structure of alternating magnetic and non-magnetic layers [24].

3.4. POLARIZED NEUTRON SCATTERING

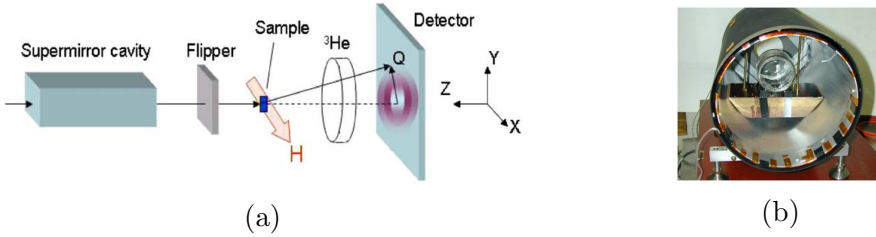


Figure 3.7: (a) Schematic of the experimental setup. From left to right the components are a polarizing FeSi supermirror, an electromagnetic precession coil flipper, sample holder with cryostat and variable magnetic field, ^3He analyzer, and a position sensitive gas detector Adapted from [39]. (b) Picture of a ^3He cell in a solenoid, from S. Watson at NIST.

This is analogous to the scattering of photons by thin films and related to the principles of total internal reflection, and Brewster's angle. If only one wavelength of neutron was required to be polarized that was always incident at the same angle extremely high polarizations could be achieved. However, a range of wavelengths incident angles need to be polarized with this supermirror, so the mirrors are designed with layers of decreasing thickness. This is in contrast to the constant thickness that would be used if only one wavelength was needed to be polarized [24]. For this work the supermirror polarized a well collimated incident beam of 5.5 \AA^{-1} neutrons. It polarized the neutrons with an efficiency of 0.95 where a polarization efficiency is defined as:

$$\left| \frac{I_{\uparrow} - I_{\downarrow}}{I_{\uparrow} + I_{\downarrow}} \right|, \quad (3.1)$$

which is the normalized absolute value of the difference between the fluxes ($I_{\uparrow}, I_{\downarrow}$) of the two spin states [39].

3.4.2 Flipper

The neutrons exiting the supermirror will always have the same polarization so in order to explore all possible spin interactions it is necessary to have a method to flip the polarization of the neutrons after the supermirror. This

3.4. POLARIZED NEUTRON SCATTERING

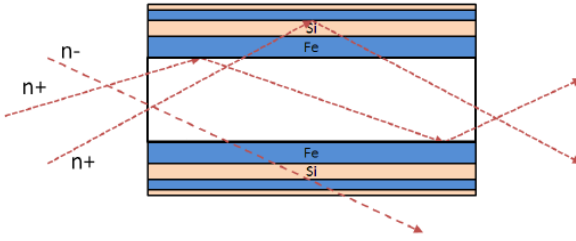


Figure 3.8: Simplified schematic of an FeSi supermirror demonstrating the preferential reflection of spin up neutrons. Image adapted from [24].

was accomplished using a radio frequency electromagnetic coil that rotates the polarization axis orthogonal to current axis and back just long enough for the Larmor precession of the neutrons to cause them end this process polarized anti-parallel to their original orientation [24]. In this work we saw efficiencies of this flipping up to 97%.

3.4.3 ^3He Analyzer

In order to be able to differentiate the scattering into the four cross sections of UU, DD, UD and, DU it is necessary to selectively pass scattered neutrons to the detector on the basis of their polarization. The ^3He cell, shown in Figure 3.7b, and others like it were used to analyze the beam polarization after scattering of the sample. ^3He has a large absorption cross section for neutrons anti-parallel to the ^3He polarization. The ^3He was initially polarized via spin exchange optical pumping, and the polarization was monitored via *in situ* nuclear magnetic resonance (NMR). The polarization of the ^3He was flipped via the application of a pulsed field allowing the selective absorption of spin up or spin down neutrons. The polarization was maintained by keeping the sample in field of about 50 G produced by a solenoid. This setup results in an exponential decay of the ^3He polarization with a time constant between 250 and 300 hours.

3.5 Sample Conditions

In order to fully explore the possible states of the MnFe₂O₄ nanoparticles under an applied field scattering experiments were conducted over multiple trips to NIST, and under in a variety of conditions for the sample. As data from different dates was ultimately scaled to eliminate the effect of variation in reactor flux the distinguishing factors between different data sets are the temperature and the applied magnetic field \vec{H} . In Table 3.1 there is a grid of the conditions taken over the temperature range of 10 - 400 K and .05 - 1.4 ± .05 T. Measurements were made at temperatures less than the room temperature through use of closed-cycle refrigerator capable of reaching temperatures as low as 5 K and a heating element to reach to 400 K, an electromagnet provided magnetic fields from 0 to 1.4 T.

	400 K	300 K	200 K	10 K
1.4 T	X	X	X	X
.3 T	X	-	-	X
.2 T	X	X	X	X
.1 T	X	-	X	X
.05 T	X	-	X	X

Table 3.1: Tabulation of the field and temperature combinations under which PASANS data were taken. "X" indicates a combination of temperature and field that was used while "-" indicates that that combination of conditions was not used.

3.6 Data Treatment

The raw data was processed using the NIST Center for Neutron Research IGOR Pro macros created by Kline [49]. The first step was to take the four cross sections and account for inefficiencies in the polarization mechanisms. The following procedure summarizes what is presented in [39] and follows the discussion in [23].

3.6. DATA TREATMENT

There are three sources of imperfection in the polarization analysis as none of the supermirror, flipper, and ^3He filter are perfectly efficient. In fact the polarization of the ^3He filter decays exponentially with time. The polarization of the ^3He filter followed

$$P_{He}(t) = P_0 e^{-t/\Gamma}, \quad (3.2)$$

where t the elapsed time, P_0 the initial polarization and Γ is the relaxation time. A typical value for P_0 was .85, while Γ ranged from 150 to 300 hours depending on the configuration of stray magnetic fields. With collection times for a single field and temperature combination of 12 hours it is necessary to explicitly include this decay of the polarization ^3He cell to accurately correct for polarization inefficiencies. To this end we define the time-dependent majority/minority spin transmission as

$$T(t) = T_e e^{-(1 \pm P_{He}(t))l}, \quad (3.3)$$

with empty cell transmission, T_e of 0.86-0.87 and opacity, l , of 2-3 depending on the specific cell used. The opacity is included to account for the neutrons of the majority transmitted spin that were absorbed. Throughout neutron absorption measurements were made and the exponential curves were fit in order to determine $P_{He}(t)$. Defining $T^{\uparrow,\downarrow}$ as the fraction of spin up (\uparrow) or spin down (\downarrow) neutrons transmitted by the ^3He cell, and $N^{\uparrow,\downarrow}$ similarly for the fraction transmitted through the supermirror and flipper we can write the desired true spin-dependent cross sections I_t in terms of the experimentally measured intensities I_m as

$$\begin{bmatrix} N_{\uparrow}^{\uparrow} T_{\uparrow}^{\uparrow} & N_{\uparrow}^{\downarrow} T_{\uparrow}^{\uparrow} & N_{\uparrow}^{\downarrow} T_{\uparrow}^{\downarrow} & N_{\uparrow}^{\uparrow} T_{\uparrow}^{\downarrow} \\ N_{\downarrow}^{\uparrow} T_{\uparrow}^{\uparrow} & N_{\downarrow}^{\downarrow} T_{\uparrow}^{\uparrow} & N_{\downarrow}^{\downarrow} T_{\uparrow}^{\downarrow} & N_{\downarrow}^{\uparrow} T_{\uparrow}^{\downarrow} \\ N_{\uparrow}^{\uparrow} T_{\downarrow}^{\uparrow} & N_{\uparrow}^{\downarrow} T_{\downarrow}^{\uparrow} & N_{\uparrow}^{\downarrow} T_{\downarrow}^{\downarrow} & N_{\uparrow}^{\uparrow} T_{\downarrow}^{\downarrow} \\ N_{\uparrow}^{\uparrow} T_{\downarrow}^{\uparrow} & N_{\uparrow}^{\downarrow} T_{\downarrow}^{\uparrow} & N_{\uparrow}^{\downarrow} T_{\downarrow}^{\downarrow} & N_{\uparrow}^{\uparrow} T_{\downarrow}^{\downarrow} \end{bmatrix} \begin{bmatrix} I_t^{\uparrow\uparrow} \\ I_t^{\downarrow\uparrow} \\ I_t^{\downarrow\downarrow} \\ I_t^{\uparrow\downarrow} \end{bmatrix} = \begin{bmatrix} I_{m,\uparrow\uparrow} \\ I_{m,\downarrow\uparrow} \\ I_{m,\downarrow\downarrow} \\ I_{m,\uparrow\downarrow} \end{bmatrix}. \quad (3.4)$$

3.6. DATA TREATMENT

Subscript spins indicate the majority spin direction of the polarizing element involved, while superscript spins refer to the majority spin direction recorded by the detector. Multiplying both sides by the inverse of the left most array allows the polarization corrected I_t 's used in Section 2.3.2 to be determined directly. While calculation of the values of the T coefficients is described above, the determination of the N coefficients involves calculating the polarization of the supermirror, P_{SM} , and the flipper efficiency, P_f , where the majority spin fraction is given by $(1+P)/2$ and the minority by $(1-P)/2$. There will also be beam depolarization as a consequence of the environment, such as stray magnetic fields. The environmental depolarization is captured within χ_D , and can be coupled to the effective supermirror polarization by $P'_{SM} = (1 - \chi_D)P_{SM}$. Thus we can write

$$N_{\uparrow}^{\uparrow} = \left(\frac{1 + P'_{SM}}{2} \right), \quad (3.5)$$

$$N_{\uparrow}^{\downarrow} = \left(\frac{1 - P'_{SM}}{2} \right), \quad (3.6)$$

$$N_{\downarrow}^{\uparrow} = \left(\frac{1 - P_F P'_{SM}}{2} \right), \quad (3.7)$$

$$N_{\downarrow}^{\downarrow} = \left(\frac{1 + P_F P'_{SM}}{2} \right), \quad (3.8)$$

where \uparrow is the implied majority neutron orientation after passing through the supermirror. P'_{SM} and P_F can then be solved for giving:

$$P'_{SM} = \frac{(T_+^+ + T_+^-) - (T_-^+ + T_-^-)(\frac{I_{m,++}}{I_{m,+-}})}{(T_-^+ - T_-^-)(\frac{I_{m,++}}{I_{m,+-}}) - (T_-^+ + T_+^-)}, \quad (3.9)$$

$$P_F = \frac{1}{P'_{SM}} \frac{(T_-^+ + T_-^-) - (T_+^+ + T_+^-)(\frac{I_{m,--}}{I_{m,-+}})}{(T_+^- - T_+^+)(\frac{I_{m,--}}{I_{m,-+}}) - (T_+^- + T_-^+)}. \quad (3.10)$$

Using the above equations it is possible to correct for inefficiencies in the polarization that might manifest as scattering intensity being incorrectly classi-

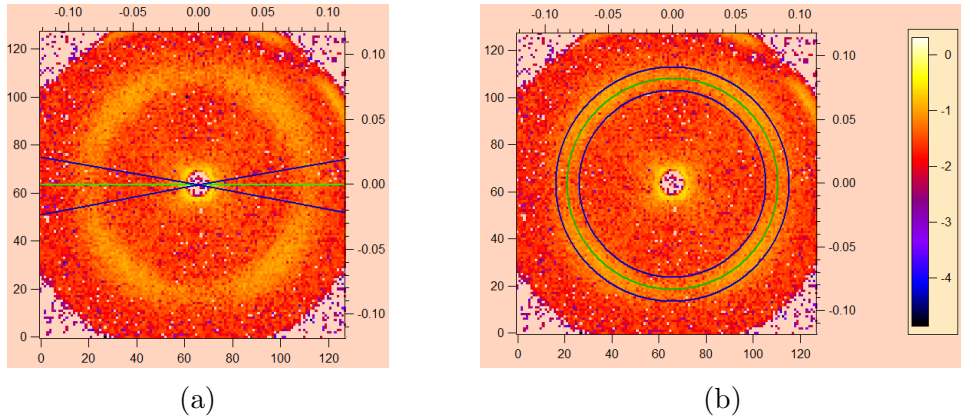


Figure 3.9: (a) Demonstration of a sector average with $\Delta\theta = 20^\circ$ with 10 degrees on each side. This gives a 1-D intensity vs Q curve. (b) An annular average centered around a Q value with the averaging extending out ± 10 detector pixels. This will return at 1-D intensity vs θ curve, with $\theta = 0$ along the positive X axis. In both types of average the central green line is the nominal angle or Q value and the blue lines denote the extent of data included in the average, and the ticks along the X and Y axis represent detector pixels

fied. These corrections were applied to the data with use of the NIST IGOR Pro SANS macros [49], and the data were transformed into 2-D cross sections UU, DD, UD, and DU for each of the field and temperature conditions. These cross sections were then used to generate the Fourier transforms of the nuclear scattering $|N|^2$, magnetic scattering parallel to \vec{H} ($|X_1|^2$ and $|X_2|^2$), and magnetic scattering due to the components of moments perpendicular to \vec{H} ($|Z|^2$, and $|YZ|^2$) on the basis of Eqs 2.18 - 2.22. While those equations call for intensity of scattering at specific angles such as 0 and 90 degrees, in practice it is necessary to include a larger slice of data. As demonstrated in Figure 3.9a the values used were actually the averages of the intensities within $\theta \pm 10^\circ$.

After applying the correction we expect that the intensity as a function of θ at a given Q should be equal for the DU and UD cross-sections. However, as shown in Figure 3.11a, we found such annular averages, Figure 3.9b, to

3.6. DATA TREATMENT

be dramatically different for DU and UD at and around the Q values corresponding to the Bragg peak in the spin flip data to be discussed in section 4.3. In contrast to the post correction data the annular averages of DU and UD in the uncorrected (RAW) data, shown in Figure 3.11b, were essentially equal at the peak Q value. This leads us to conclude that the discrepancy is the result of the polarization correction we are applying being too dramatic at and around the peak. This is reasonable as the correction factor that was applied at every Q value was determined from data sets that are dominated in intensity by the lower Q regions of the data. If, however, the sample has a Q dependent effect on the polarization then applying a uniform correction may no longer be valid. The Bragg peak (see section 4.3) present in the magnetic scattering of this sample can polarize the neutron beam in a manner similar to the supermirror, resulting in the polarization at Q values around the peak Q being different from the polarization at low Q. In order to resolve this we corrected different Q ranges of the data differently, at low Q values we used the original correction, and at higher Q values around the peak we determined a new polarization value, corrected the data a second time and then spliced the data together. This is generally a reasonable course of action as the supermirror and other polarizing elements are designed to be wavelength and Q agnostic.

In practice changing the polarization used to correct the data is not enough to eliminate the DU/UD discrepancy, and even at the lower Q values there remains a small difference after correction. Given this, we chose to use annular averages of the quantity

$$dDU \equiv \frac{DU - UD}{DU + UD} \quad (3.11)$$

as an evaluative metric for the quality of the new polarization around the peak. The aim is to find a polarization such that dDU at the peak for the new polarization will be equal to the dDU values at low Q for the original polarization values used. If we then take this newly corrected data, we can

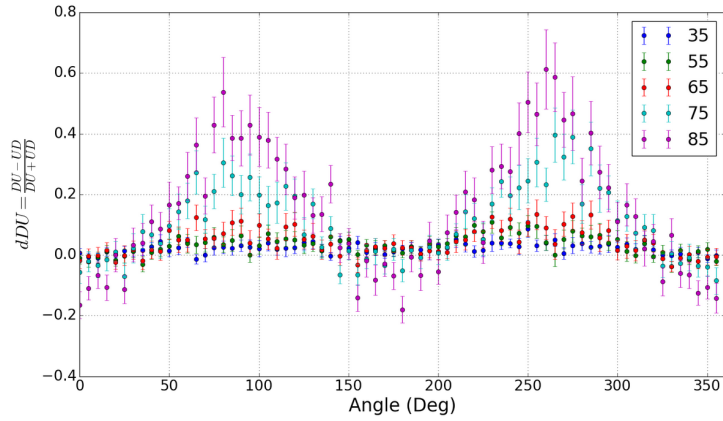


Figure 3.10: Variation of dDU with angle for 0.05 T at 10 K. The legend is $Q \times 1000$ with values ranging from 0.035 to 0.085 \AA^{-1} . Note that $dDU(0.085 \text{\AA}^{-1}) \neq dDU(0.055 \text{\AA}^{-1})$

splice it together with the original correction in order to have a consistent dDU across the entire Q range. As with 0.05 T at 400 K, shown in Figure 3.10, the conditions with a peak have a consistent increase in dDU with increasing Q.

3.6.1 Determining Peak Polarization Values

To determine the optimal polarization values to use around the peak we corrected the data with several values. We then compared the value of dDU at the peak (0.085\AA^{-1}) and used the polarization that had that best match the dDU of low Q for the original correction. We chose to compare to either $Q = 0.035 \text{\AA}^{-1}$ or 0.055\AA^{-1} based on the error bars and whether $dDU(0.055 \text{\AA}^{-1})$ was significantly different than $dDU(0.035 \text{\AA}^{-1})$ for the original polarization. Using this method we were able to find a polarization value that would give a good match between $dDU(0.085 \text{\AA}^{-1})$ of the new polarization and $dDU(\text{low } Q)$ for the original polarization.

3.6. DATA TREATMENT

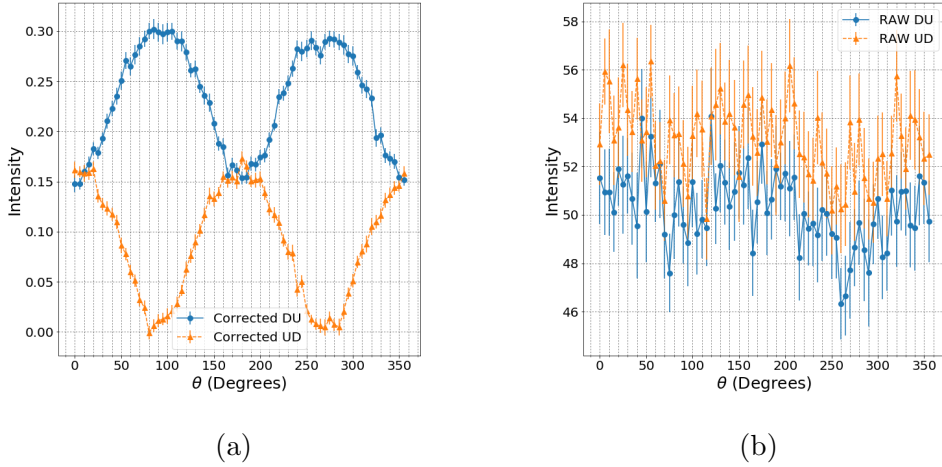


Figure 3.11: Annular averages at $Q = .085 \text{ \AA}^{-1}$ for $0.2 \text{ T } 10 \text{ K}$ data. (a) Comparison of DU and UD annular averages after the original polarization correction, there is a dramatic and unexpected difference between them. (b) In the data prior to the polarization correction(RAW) the dependence on θ of the intensity at $Q = .085 \text{ \AA}^{-1}$ is the same for both the DU and UD spin flip cross sections. Data were collected with $\vec{H} = 0.2 \text{ T}$ at 10 K .

3.6.2 Data recombination

After this correction all the data are still in 2D format and there are the two sets of data with different polarization corrections. For each of these sets all the 1D quantities we are concerned with ($|N|^2$, $|X_1|^2$, $|X_2|^2$, $|YZ|^2$, $|Z|^2$) were calculated. Then using the NSort panel of the NIST SANS macros [49] the low Q data with the original correction and the data around the peak with the new correction were combined as in Figure 3.12 with no additional adjustments such as scaling. Ideally there would be a variety of different polarization used on the data between the peak and the lower Q data in order to better approximate a continuous change in the polarization. Unfortunately the level of granularity of our data does not allow for this. Consequently, we applied just two corrections which resulted in small discontinuities in the new combined data; however, the new combined data will still be more accurate to use for the analysis of the data.

3.6. DATA TREATMENT

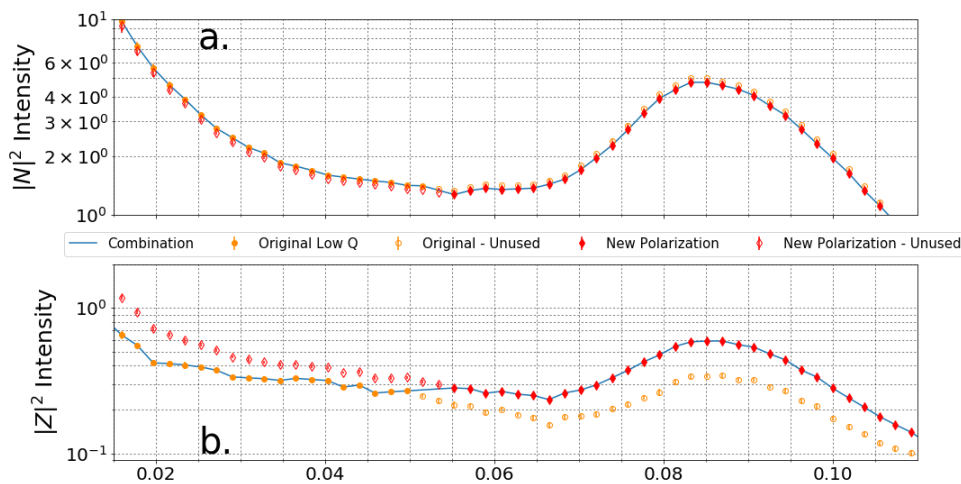


Figure 3.12: Combining the original June RF 10 with the peak data after the correction matching dDU was applied. Red Diamonds are the data with the correction matching the dDU values and the orange circles are the original correction. The solid points as traced by the line were used for the combined data used for analysis. (a) The new correction has a minimal effect on the $|N|^2$ intensity which is derived from the DD and UU cross sections. (b) In contrast, the $|Z|^2$ intensity, which is derived from the UD and DU cross sections, has a significant difference in this new correction.

Chapter 4

Results

4.1 Structural $|N|^2$ Scattering

The $|N|^2$ or structural component is highly similar across all field and temperature conditions. As can be seen in a plot of representative conditions, Figure 4.1, we observe a Bragg peak related to interparticle coherent scattering at $Q = .085 \text{ \AA}^{-1}$.

These data match the scattering expected from an FCC-Paracrystal model described in [47]. However, fitting is not straightforward due to the non-uniform distribution of manganese in the nanoparticles requiring a model incorporating both a core and shell. Using the SasView platform [50], Hillary Pan has developed such a model which computes the scattering from an FCC crystal in which the scatterer at each lattice site is a nanoparticle composed of a core and shell. Based on the EELS work, the radius of the core was chosen to be 32.5 \AA and the thickness of the shell as 5 \AA . As the core is very Fe rich, a value of $7 \times 10^{-6} \text{ \AA}^{-2}$ was used as the scattering length density (SLD) for the core. The shell is Mn rich, but also contains some Fe, so we expect the SLD of the shell lie between 1.5 and $5 \times 10^{-6} \text{ \AA}^{-2}$ which are the SLDs of Mn_3O_4 and MnFe_2O_4 respectively. Using a value of $4 \times 10^{-6} \text{ \AA}^{-2}$ for the shell SLD and fitting to other parameters including scaling factors, the

4.2. MAGNETIC $|X|^2$ SCATTERING

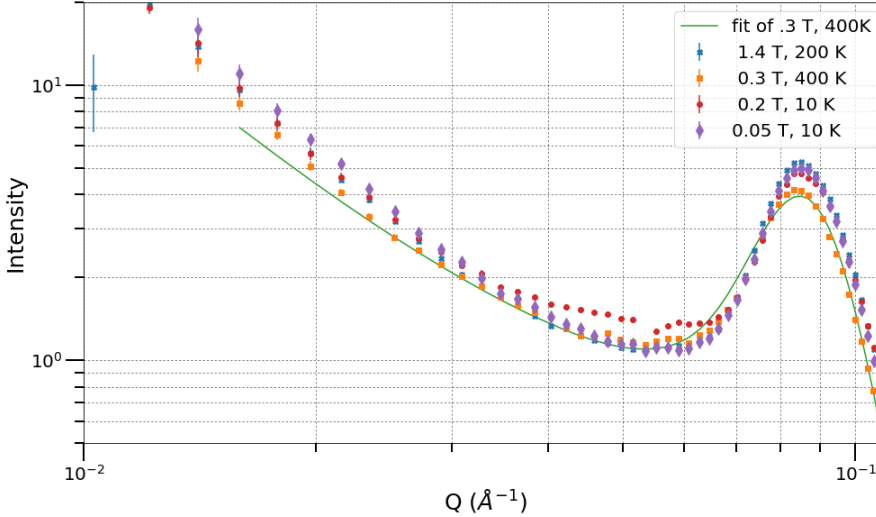


Figure 4.1: Representative plot of the structural conditions. Note the consistency between conditions and the peak at $Q = .085 \text{ \AA}^{-1}$. For clarity only a fit of .3 T at 400 K has been included but in general, there is good agreement between fits and the data.

background, and nearest neighbor distance results in fits of the structural data that are consistent with the earlier characterization of the particles.

The model of FCC-paracrystal with scatterers as a core-shell particles is effective at capturing the FCC lattice parameters; however, it is less accurate at lower Q values. In order to fix this, work is being put into adding the scattering from independent core-shell particles to the structural scattering. Such an addition would capture particles that do not align with the lattice in the same way as a consequence of lattice defects. The main takeaway from the structural scattering is that it behaves as expected given the other characterization work.

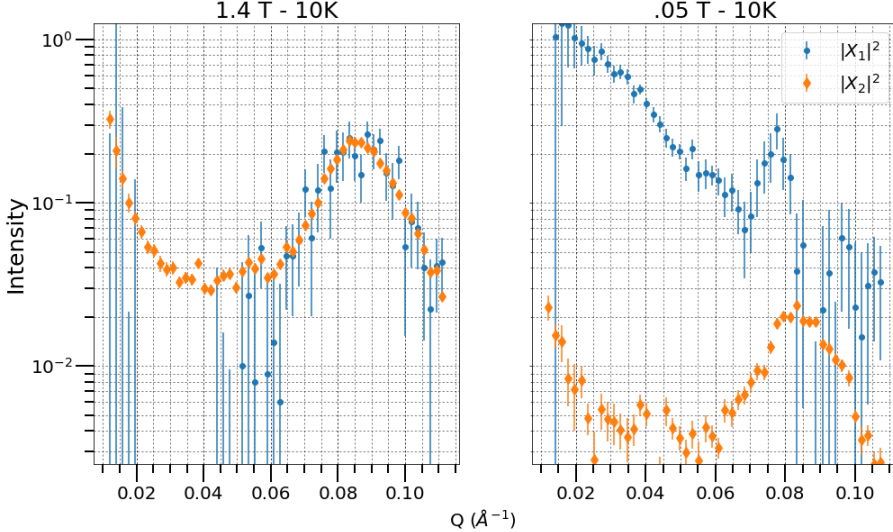


Figure 4.2: (Left) In high applied field, $|X_1|^2$ matches up closely with $|X_2|^2$ as the majority of the X component of scattering is in phase with the structural scattering as seen from eq. 2.20. (Right) However, in remanent field, $|X_2|^2$ does not comprise of a majority of $|M_X|^2$.

4.2 Magnetic $|X|^2$ Scattering

The component of magnetic scattering along the applied axis, $|X|^2$, was calculated via both $|X_1|^2$ and $|X_2|^2$ (Eqs. 2.19, 2.20) which access that component through different manipulations of the DD and UU cross sections. The $|X_1|^2$ data captures the entirety of the magnetization parallel to \vec{H} ; however, it is calculated via the subtraction of two sector averages of the 2D data and consequently has large error bars. In contrast $|X_2|^2$ has relatively small error bars as it is calculated through a division, although it does not capture the same thing as $|X_1|^2$. $|X_2|^2$ is only the component of parallel magnetic scattering that is in phase with the nuclear scattering as seen from eq. 2.20. As shown in Figure 4.2, in large applied fields $|X_1|^2 = |X_2|^2$ while in remanent fields $|X_2|^2$ is much less than $|X_1|^2$. This is because in a high applied field,

4.3. MAGNETIC $|Z|^2$, $|YZ|^2$ SCATTERING AND $\frac{|YZ|^2}{|Z|^2}$

the nanoparticles form large domains, and the majority of spins align with the applied field such that the field aligned magnetic scattering is coherent with the nuclear (structural) scattering. In low applied field, the majority of $|M_X|^2$ comes from uncorrelated spheres, and we see a shape in $|X_1|^2$ more similar to single sphere scattering.

As illustrated in Figure 4.3, in $|X_2|^2$ we can clearly see a Bragg peak at the same Q as in the $|N|^2$ correlations as expected. Unlike $|N|^2$, the intensity of $|X|^2$ is highly dependent on the sample temperature and the applied field. The intensity is greater at higher field and lower temperature, overall following a story of higher fields and lower temperature resulting in larger domains and greater intensity.

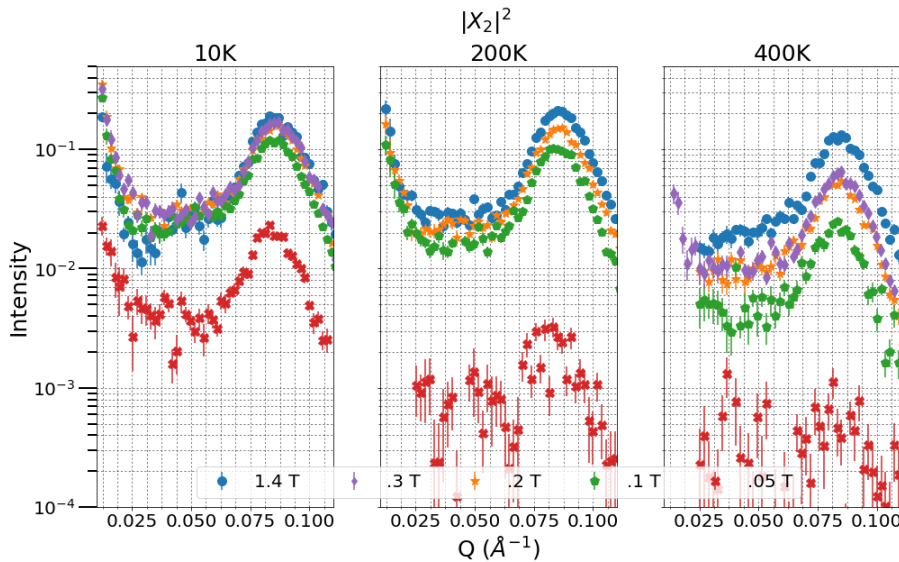


Figure 4.3: Comparison of $|M_X|^2$ across temp and field.

4.3 Magnetic $|Z|^2$, $|YZ|^2$ Scattering and $\frac{|YZ|^2}{|Z|^2}$

While the structural scattering and magnetic scattering from the component of magnetization parallel to the field are consistent with our expectation, we

4.3. MAGNETIC $|Z|^2$, $|YZ|^2$ SCATTERING AND $\frac{|YZ|^2}{|Z|^2}$

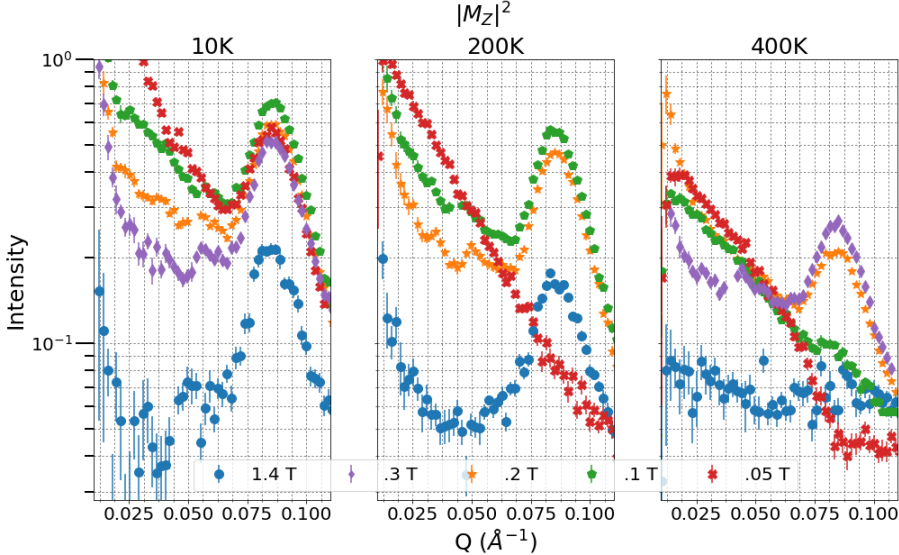


Figure 4.4: Comparison of $|Z|^2$ across temp and field.

find many unusual features when considering magnetic scattering due to the projection of magnetic moments onto other axes. In Figure 4.4, we plot the $|Z|^2$ scattering for a variety of fields and temperatures. Surprisingly, in many of the conditions, there is a $Q = 0.085 \text{ \AA}^{-1}$ peak which was not observed in the CoFe_2O_4 or Fe_3O_4 nanoparticles discussed in Section 2.4. This peak indicates the presence of a significant coherence over multiple nanoparticles of the component of moments perpendicular to the applied field, this holds even in conditions of high field and low temperature. The $|Z|^2$ is at the same Q location as the peak in $|N|^2$ and $|M_X|^2$. At both 10 K and 200 K, the peak intensity is maximized in the 0.1 T condition while at 400 K the peak is maximized in the 0.3 T condition. We can interpret this as there being some interparticle coupling occurring in an applied field that tends to align the portions of moments of the nanoparticles along the Z axis i.e. parallel to the applied field.

For fixed field, increasing temperature primarily results in a reduction in scattering associated with the overall decrease in moment and with the

4.3. MAGNETIC $|Z|^2$, $|YZ|^2$ SCATTERING AND $\frac{|YZ|^2}{|Z|^2}$

higher temperature tendency to disorder a given structure. Looking at fixed temperature the behavior as a function of field varies in a more complex fashion; presumably as a result of interparticle domain formation.

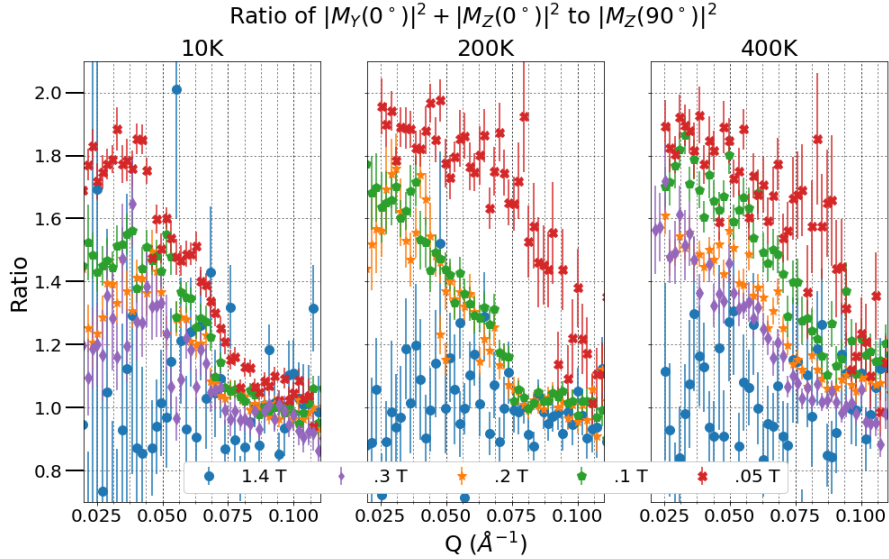


Figure 4.5: Comparison of $\frac{|YZ|^2}{|Z|^2}$ across temp and field. A Priori we would expect that the Ratio would have a uniform value of 2 across all Q values regardless of applied field or temperature, however, the results here deviate significantly from that. Higher applied fields keep the ratio closer to 1, and higher temperatures tend to spread out the Ratios of different fields. The data have a tendency to reach a Ratio value of 1 around the location of the interparticle peak in $|N|^2$ that corresponds to the lattice spacing of the particles.

If the scattering is isotropic, then given a peak in $|Z|^2$, there should also be a peak in $|Y|^2$. Unfortunately we cannot extract $|Y|^2$ easily from our data without assuming that $|Z|^2$ is independent of angle θ , an assumption we have been unable to make with our data, a conclusion supported by recent computational studies [51] demonstrating $|Z|^2$ scattering with a θ dependence. Instead we can study the ratio of horizontal and vertical slices of the spin flip scattering, $\frac{|YZ(0^\circ)|^2}{|Z(90^\circ)|^2}$, henceforth described as the ratio, which reduces to

4.4. MODEL AND MODEL RESULTS

$\frac{|Y|^2+|Z|^2}{|Z|^2}$ if $|Z(90^\circ)|^2 = |Z(0^\circ)|^2$. Taking into account the symmetries of the system, we would also expect $|Y|^2 = |Z|^2$ resulting in a ratio of 2 at all values of Q. In Figure 4.5, we see that the ratio deviates significantly from 2 in all temperature and field conditions; with the ratio value and Q location of the falloff to one dependent on the strength of the applied field and sample temperature. At 10 K, the ratio scattering is noisy but 1 for all Q at 1.4 T, indicating that the Y and Z components of magnetization are completely correlated within the structure. For other conditions the ratio is higher at low Q, then drops to 1 when as Q is increased. At 200 K we see the same trend with field but the data are more spread out. In particular at remanence the ratio tends to be much higher at all Q values and the dropoff to 1 for 0.1 and 0.2 T is pushed to higher Q values. A similar effect is observed in the 400 K data.

Given the results from similar studies of CoFe_2O_4 , and Fe_3O_4 nanoparticles, it is not unexpected to see that a portion of the magnetic moments of the manganese ferrite nanoparticles canted off the field axis. The dramatic result is that the scattering from the components of the moments along Y and Z axes is coherent between nanoparticles as evidenced by the peak in $|Z|^2$. The differences between coherent and incoherent canting are illustrated in Figure 4.6; the ordering in (b) of that Figure implies that there are inter-particle interactions playing a significant role in this system. In addition, the effect is present not just in the peak data but also in the scattering at other Q, given the deviation of the ratio from the uncorrelated value of 2.

4.4 Model and Model Results

As the behavior described in Section 4.3 is quite unusual we don't expect to be able to use the standard scattering models such as those incorporated into SasView. There is thus a need to come up with a different representation of the system and to also either explicitly or implicitly incorporate \vec{H} and

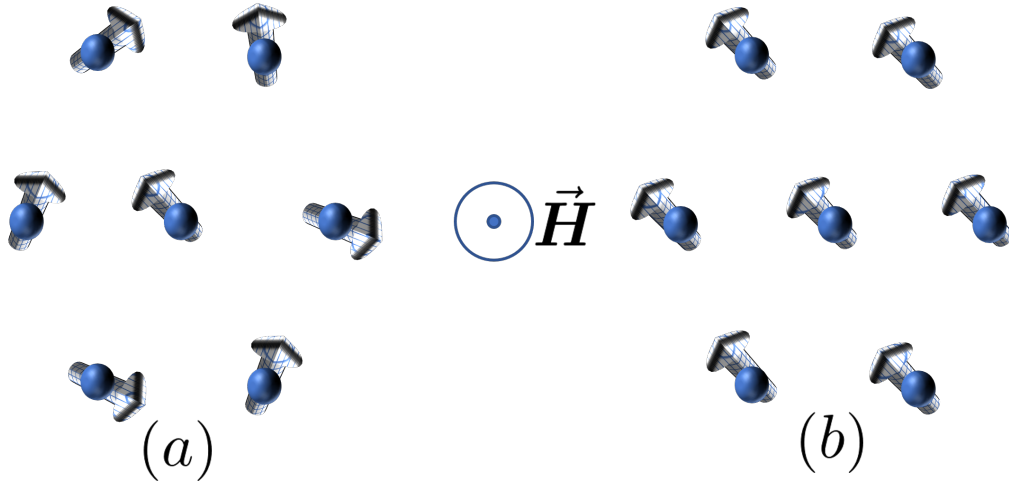


Figure 4.6: Illustrations of (a) incoherent canting of nanoparticle spins. The spins are all canted off the field direction however they are not correlated and neutron scattering of this assembly would not produce a peak in the $|Z|^2$ or $|Y|^2$. In contrast the arrangement in (b) in which the spin all cant in the same way would result in coherent scattering from the magnetization components perpendicular to the field. For both diagrams the applied field \vec{H} is out of the page.

the temperature. To this end our NIST collaborator Dr. Krycka has been developing an energy-based model to explain the Q dependence of the ratio of the vertical to horizontal spin flip scattering.

4.4.1 Model Explanation

As described in [52], this model consists of stacked layers of nanoparticles in a hexagonal close packed arrangement. With individual layers, depicted in Figure 4.7a, consisting of nanoparticles placed on a hexagonal grid. This arrangement results in 6 possible easy axes to be considered when calculating the anisotropy energy. Importantly, this anisotropy energy is not related to the intra-nanoparticle spinel structure; rather it is a consequence of the hexagonal close packing and dipolar nanoparticle interactions.

4.4. MODEL AND MODEL RESULTS

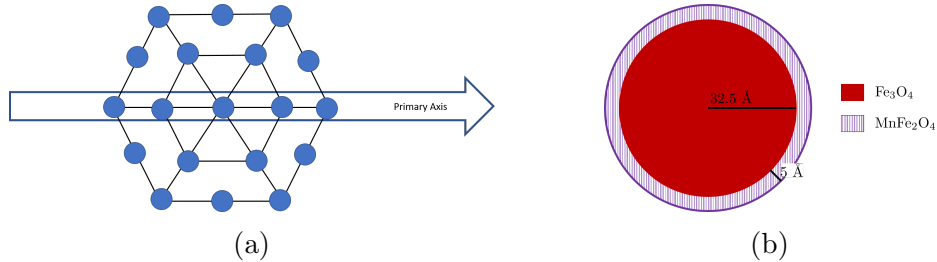


Figure 4.7: (a) Depiction of a single hexagonal close packed layer of nanoparticles. The blue spheres represent nanoparticles and are placed on a hexagonal grid with the nanoparticle-nanoparticle spacing determined as an input to the model with a typical value of 83 Å, in agreement with the interparticle spacing from the structural data discussed in Section 4.1. (b) Depiction of the nanoparticle used in the model developed by our collaborator Kathryn Krycka. The nanoparticle is built out of a core and two shells in order to approximate the continuous change in manganese concentration revealed by EELS.

Reflecting the EELS characterization discussed in Section 3.2, the individual nanoparticles are not chemically uniform. As depicted in Figure 4.7b, they are modeled as consisting of a Fe_3O_4 core and an outer shell composed of MnFe_2O_4 . While the nanoparticles used for this model have a chemical core-shell, there is not a magnetic core shell as there was in the Fe_3O_4 model. While this could be implemented, we suspect that we do not have sensitivity to the effects of this, so the addition of such a feature would not improve our explanatory power.

Several layers are stacked together as in Figure 4.8a and the whole assembly is rotated over all space with the angles defined in Figure 4.8b. As the layers are rotated, the scattering for each position is calculated and the results are summed, recalculating the direction and magnitude of nanoparticle moments at each step. Without the influence of an applied magnetic field or a significant magnetocrystalline anisotropy, dipolar coupling would be the driving force in determining moment direction. In that situation, the moments of particles in a layer would all line up along a randomly chosen

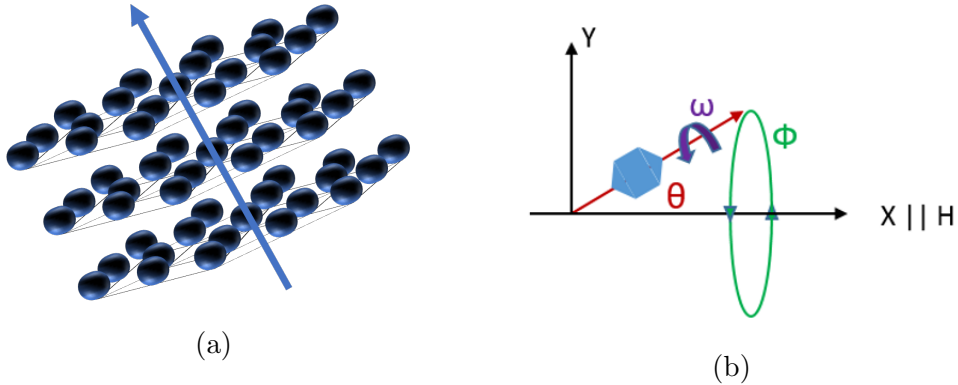


Figure 4.8: (a) Side view of a group of stacked layers. The arrow represents the stacking direction, which can be oriented along any vector. (b) Rotations that layers of nanoparticles are put through in order to calculate the scattering. The angles have domains of $\theta \in [1, 89^\circ]$, $\Phi \in [0, 360^\circ]$, $\omega \in [0, 90^\circ]$ in steps of 2° , 8° , and 15° , respectively.

one of the six symmetry axes of the hexagonal arrangement. Implementing random selection results in the originally expected 2 to 1 ratio of the vertical and horizontal spin flip intensities. In order to capture a ratio of 1 at the peak location and elsewhere, the model is modified so that the symmetry axis of the hexagonal layer that is closest to \vec{H} is used as the axis onto which a purely dipolar interaction would cause the nanoparticle moments to align. The angle the moments will assume between the best in plane easy-axis and \vec{H} is then determined via a minimization of the dipolar and Zeeman energies. Repeating this process and applying the Halpern-Johnson spin selection rules allows for the calculation of the total spin flip (\mathbb{C}) and non spin flip (\mathbb{A}) scattering as a function of Q for $\theta = 0, 90^\circ$.

4.4.2 Model Results

There are many standard parameters in this model such as the nanoparticle radius and the nanoparticle to nanoparticle spacing, which, while important, are fixed by our previous data and do not require further explanation. The parameters we have explored varying so far in order to match the magnetic scattering data include: number of scattering centers, number of layers, radius of magnetic core, magnetic SLD, fraction of pinned spins (separate for nuclear and magnetic).

The number of scattering centers describes the number of nanoparticles included in a layer of the stack. As of this writing, this variable is still limited to values of 39 or lower which prevents us from exploring the effects of creating very large domains. The number of layers is best described by its name; while we have varied it in the hopes of affecting the magnetic scattering predicted by the model, we have found that it primarily affects the structural scattering. The magnetic radius describes the radius of the nanoparticle core that the model assumes is magnetic. The magnetic SLD describes the SLD of that core with a maximum expected value of $1.46 \times 10^{-6} \text{ \AA}^{-2}$ for Fe_3O_4 . However, we expect a lower magnetic SLD as there will also be manganese included in the radius of the core. Furthermore, based on the hysteresis measurements performed, as shown in Figure 3.4, we expect a softening of the magnetic moment with temperature and can account for this via a reduction of the magnetic SLD. This is not explicitly included in the model, so we vary the SLD parameter by hand to try to capture this for data at different temperatures. The fraction of pinned spins represents the fraction of the nanoparticles that do not easily align with \vec{H} or other nanoparticle spins. These pinned spins occur as a result of lattice defects, so we expect this variable to be small and not to vary with changing temperature or field, and so do not have great freedom in how much we vary this parameter.

As demonstrated in Figure 4.9, the model captures the most important aspects of the data at .05 T, 400 K. Namely, the model does not produce a

4.4. MODEL AND MODEL RESULTS

peak in the SF scattering and follows the trend of the ratio with Q . Moving to Figure 4.10, we see that in a condition such as 0.2 T at 400 K the model can accommodate a peak in the SF scattering and still capture the ratio well. This is a significant applied field; however, given the high temperature and still fairly low strength of \vec{H} , we do not expect large domains to form. So at a temperature that is large relative to the blocking temperature, we see that the model does a good job of capturing the major features of the data. However, moving to 1.4 T at 200 K, shown in Figure 4.11, a condition in which we expect the formation of sizable domains, we see that the model fails to capture the data. In high field and low Q the magnitude of $|Z|^2$ is reduced relative to lower field conditions because spins tend to align more with \vec{H} leaving a smaller component of the magnetic moments perpendicular to \vec{H} . However, we should expect large domains of correlated particles, to form giving rise to a peak in $|Z|^2$. Currently the model is unable to capture this combination of factors, and we believe that this is due to the number nanoparticles per layer currently being limited to 39. In short, the model has been successful in capturing the data for conditions with expected small magnetic domains, but not those with large domains.

4.4. MODEL AND MODEL RESULTS

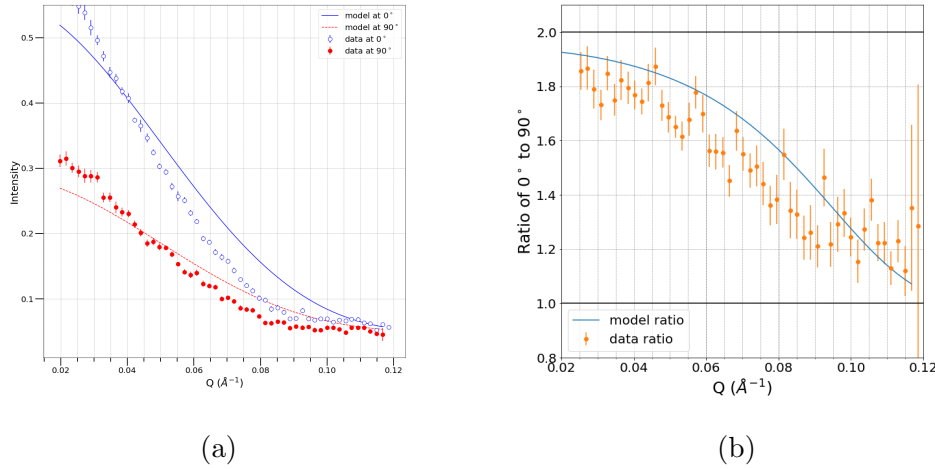


Figure 4.9: Result of the model for 0.05 T and 400 K. (a) Comparison of the model's simulated spin flip (SF) scattering vs the data, 90 Degrees corresponds to $|Z|^2$ and 0 degrees to $|YZ|^2$, demonstrating that the model is robust to conditions that do not have a peak in $|Z|^2$. The match is not perfect, but this demonstrates that the model is able to give a strong qualitative description of this field and temperature extreme. (b) Result of the ratio compared to the data for 0.05 T at 400 K, overall the model has captured the shape of the data.

4.4. MODEL AND MODEL RESULTS

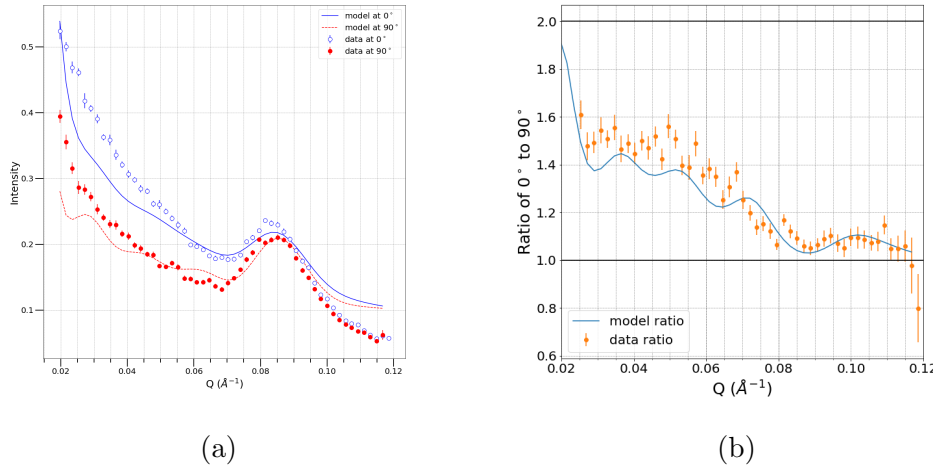


Figure 4.10: The results of the model for 0.2 T and 400 K (a) Comparison of the model's simulated spin flip scattering at 0 and 90 degrees to the data. Demonstrating that the model is capable of reproducing a peak in $|Z|^2$ and $|YZ|^2$. (b) Comparison of the ratio calculated by the model with the data. The data are more smeared than the model, resulting in the model curve appearing bumpier than one might expect. Overall, there is fairly good agreement between both the spin flip and scattering the ratio.

4.4. MODEL AND MODEL RESULTS

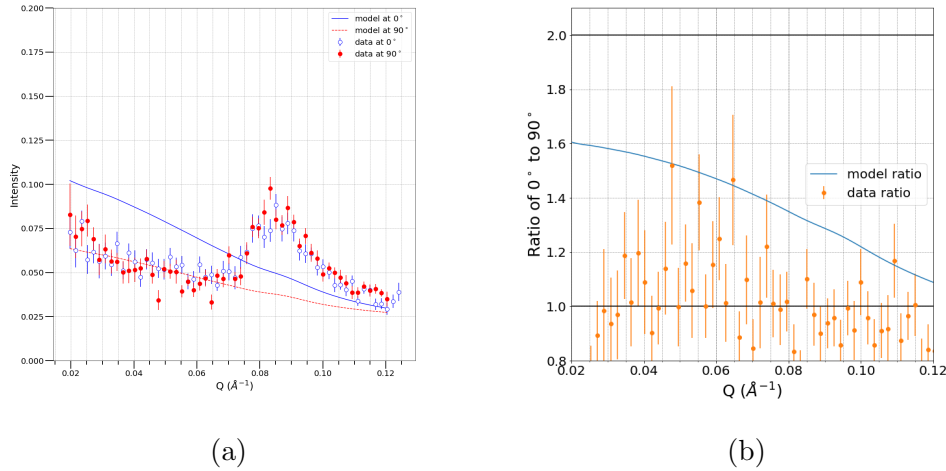


Figure 4.11: The results of the model for the conditions of 1.4 T and 200 K (a) Comparison of the model's simulated spin flip scattering at 0 and 90 degrees to the data. In this large of a field the model is not capable of modeling the peak in the data. (b) Comparison of the ratio calculated by the model with the data. The model currently cannot create large enough domains to capture the ratio for this condition.

Chapter 5

Summary and Future Work

5.1 Summary

This thesis has outlined results obtained while investigating a system of manganese ferrite nanoparticles using PASANS techniques with supplemental analysis through TEM, SQUID magnetometry and EELS. This analysis has revealed a chemical core-shell structure which is surprising given that *a priori* consideration of the synthesis method would lead to an assumption of chemically uniform nanoparticles. While this would make it not unsurprising to see that the core and shell of the nanoparticles exhibit different magnetic behavior we see as well correlations between nanoparticles. These correlations are evidenced by the significant component of magnetic scattering perpendicular to the applied magnetic field, indicating important intra, and inter-particle effects. This analysis required novel data treatment protocols to account for polarization of the neutron beam by the sample. In service of this novel procedure I developed extensions to NCNR IGOR Pro SANS macros, and further code in Python to facilitate the calculation of polarization of the beam as a function of Q. The highly useful IGOR pro functions were made publicly available and may be found in Appendix A.

In order to understand the results found by PASANS, an energy based

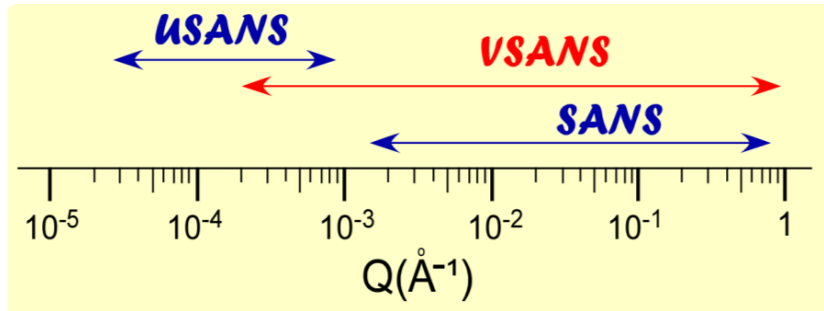


Figure 5.1: Depiction of the increased range of the vSANS image which will allow for taking more data at once than the current SANS instrument. Image taken from [53]

model is under development to understand interparticle interactions and how they might lead to the observed scattering. Early results from this model capture important features such as a non constant ratio of horizontal to vertical spin flip scattering under conditions of high temperature and low field. These results to date suggest that a model allowing for the formation of large domains will be capable of explaining the interesting scattering.

5.2 Ongoing and Future Work

There are still phenomena to explain in this manganese ferrite system and other related materials. Modeling has shown promising results in conditions for which we expect small domain sizes, but, the model needs to be expanded to allow larger domain sizes. With this improvement we hope to be able explain all of the conditions for which we have data and understand how the interparticle coupling leads to a peak in $|Z|^2$.

The PASANS work to date has focused on a limited Q range up to 0.12 \AA^{-1} . For Fe_3O_4 , CoFe_2O_4 , and manganese ferrite nanoparticles, only one major feature (such as a dip, falloff, or peak) has been evident which has limited data interpretation. However, plans for larger ${}^3\text{He}$ cell polarizers and solenoids are underway which should nearly double the maximum Q range

5.2. ONGOING AND FUTURE WORK

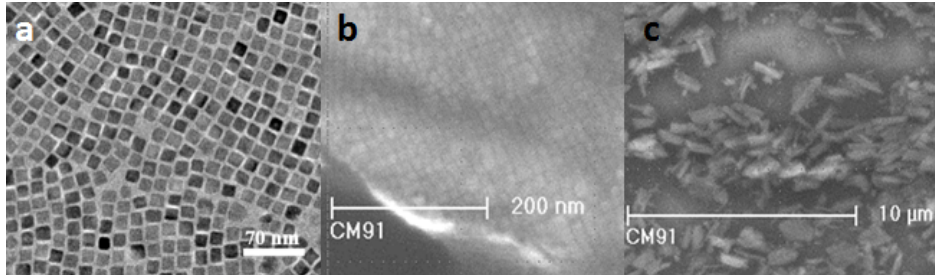


Figure 5.2: TEM and SEM images of iron oxide nanocubes. (a) TEM of a 2D array; (b) SEM of part of a 3D nanobelt made of nanocubes; (c) SEM showing multiple 3D nanobelts in a powder sample. Images from Dr. Majetich and her students.

to 0.20 \AA^{-1} . Such a change will allow several other ordering peaks to come into view for crystallized nanoparticle systems of similar sizes. There are also more ambitious plans for an in-situ apparatus so that the ^3He analyzer can be optically pumped while on the neutron beamline, thereby maintaining high polarization efficiency throughout a scattering experiment [54]. Another SANS instrument of interest for future work is the in-construction vSANS or very Small Angle Neutron Scattering spectrometer, which as demonstrated in Figure 5.1 will allow for a larger scattering range of data (2×10^{-4} to 1 \AA^{-1}) [53]. These instrumentation improvements will also facilitate faster data collection on new systems, and a deeper exploration of the systems

Looking beyond systems of ferrite nanoparticles future work will also focus on systems that introduce shape anisotropy as a new energy consideration such as self assembling magnetite nanocubes [55], for which preliminary characterization work can be seen in Figure 5.2. The shape anisotropy along with the self assembly behavior suggests that there are complex magnetic structures to be explored in this system. As demonstrated by this thesis and other works PASANS is a powerful technique for analyzing magnetic structure so future work could focus on the study of nanocubes.

Appendix A

Custom IGOR Pro Analysis Macros

At various points in the analysis that went into this thesis we wanted to average over θ at multiple Q values and compare the results. Doing this using the standard NIST SANS Macros is very time consuming and carries the risk of misnaming a file. In light of this I, along with Hillary Pan, wrote a set of IGOR Pro macros entitled OC SANS MACROS, the interface of which can be seen in Figure A.1. The functions piggyback on the NIST macros functionality and abstract it to a higher level allowing the user to rapidly perform averages over many Q values for a single set of 2D data. The program also saves the files in a consistently named manner based on user input. Beyond the ability to rapidly do multiple different averages to enable faster analysis of data, these macros also include a functionality to calculate $|N|^2$, $|X_1|^2$, $|X_2|^2$, $|Z|^2$, $|YZ|^2$, and the ratio of $|YZ|^2$ to $|Z|^2$. To calculate all of those quantities manually is a time-consuming and potentially error-prone process. I wrote code, which, when directed to a folder would figure out the names of the appropriate files and use them to rapidly calculate all the 1-D Fourier transform data sets of concern. This is merely a convenience for post-beam time analysis of data, but while on the beamline, it is highly

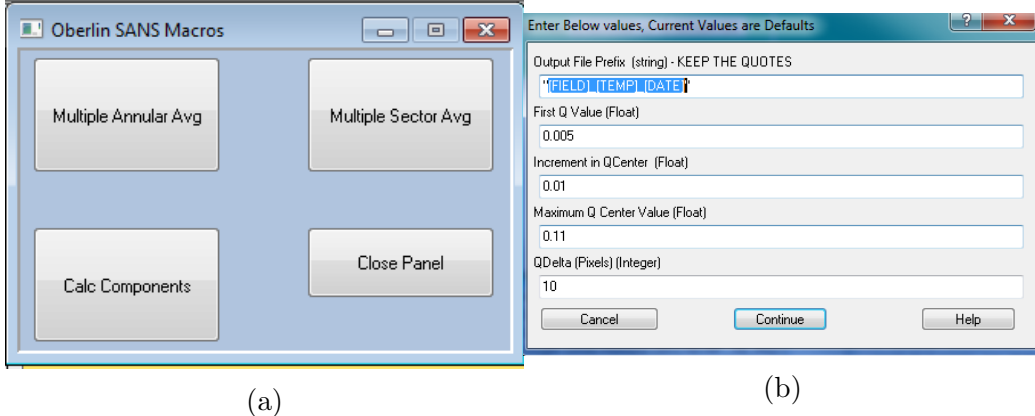


Figure A.1: (a) Panel of buttons in IGOR interface exposing the highest level functions. (b) Panel of inputs for the multiple annular average function. It is much quicker to fill out this panel and have the files autosaved than to use the standard interface.

desirable to be able to rapidly analyze the data in preparation for decisions about next sample conditions.

The OC SANS MACROS are very useful for their automation of critical yet repetitive tasks and are available on github at https://github.com/ianhi/OC_SANS_MACROS for public usage.

```

#pragma rtGlobals=3           // Use modern global access method and strict wave access.
# Place this file in WaveMetrics/Igor Pro 6 User Files/User Procedures/OC_SANS_MACROS/

//=====ACTUAL FUNCTIONS
Function MultXCalc()
    Variable Phi_Initial=0
    Variable Phi_step=15
    Variable Phi_max=180
    String Condition_info="[FIELD]_[TEMP]_[Q]"
    Prompt Phi_initial,"Initial Phi Value (Float)"
    Prompt Phi_step,"Step Size for Phi (Float)"
    Prompt Phi_max,"Maximum Phi (Float)"
    Prompt Condition_info, "Condition variables - _B[Phi] will be added automatically"

    DoPrompt "Enter Below values, Current Values are Defaults",Condition_info,Phi_initial,Phi_step,Phi_max
    if(V_Flag)
        Abort "You Cancelled - Ouch, I have feelings you know...."
    endif

    PickPath()
    PathInfo catPathName
    string A_Data=Condition_info+"_A90"
    print A_Data
    Execute "A_LoadOneDDataWith Name(\\""+S_Path+A_Data+"\\",0)"

    variable i=0
    do
        Variable Phi=Phi_Initial+Phi_step*i
        string B_Data=Condition_info+"_B"+num2str(Phi)
        Execute "A_LoadOneDDataWith Name(\\""+S_Path+B_Data+"\\",0)"
        //DO CALC=====
        MultiplyDataSets(B_Data,B_Data,1,"temp")
        variable factor = sin(Phi*pi/180)^4
        print factor
        print "B_Data: "+B_Data
        DivideDataSets("temp",A_Data,4*factor,"X2_"+Condition_info+"_"+num2str(Phi))
        fReWrite1DDData_noPrompt("X2_"+Condition_info+"_"+num2str(Phi),"tab","CRLF")
        killData("temp")
        i+=1
    while(Phi<Phi_Max)
End

Function killData(DF)
//taken from A_PlotManager_Kill in file Common/Packages/PlotManager/PlotManager_v40.ipf
{
    String DF
    String savDF=GetDataFolder(1)
    ControlInfo popup0
    SetDataFolder DF
    KillVariables/A           //removes the dependent variables
    SetDataFolder savDF
    //now kill the data folder
    KillDataFolder/Z $DF
    ControlUpdate popup0       //refresh the popup, very important if last item removed
}
End

Function MultSectAvg()

//USER VARIABLE SELECTION
Variable Phi_Initial=0
Variable Phi_step=15

```

```

Variable Dphi=-1
Variable Phi_max=180
String side="both"
String prefix="[FIELD]_[TEMP]_[Q]_[TYPE]"

Prompt Phi_initial,"Initial Phi Value (Float)"
Prompt Phi_step,"Step Size for Phi (Float)"
Prompt Dphi,"Delta Phi Default is Phi_step/2 (Float) "
Prompt Phi_max,"Maximum Phi (Float)"
Prompt side,"Sides?",popup,"both;right;left"
Prompt prefix,"Output File Prefix (string) - KEEP THE QUOTES"
DoPrompt "Enter Below values, Current Values are Defaults",prefix,Phi_initial,
Phi_step,Dphi,Phi_max,side //Keep Prefix First as this is what will be modified every
time so its nice for user this way
if(V_Flag)
    Abort "You Cancelled - Ouch, I have feelings you know....This is so an
noying Ian -- Hillary"
endif
//END USER VARIABLE SELCTION

if(Dphi===-1) // set Dphi if user did not pick a value
    Dphi=Phi_step/2
endif

// need next two lines or wont work
SVAR type=root:myGlobals:gDataDisplayType
NVAR useXMLOutput = root:Packages:NIST:gXML_Write

String path=MultAvgSetUp() //get path and do some other set up
Variable i=0
do
    Variable Phi=Phi_Initial+Phi_step*i
    String temp="AVTYPE=Sector;PHI="+num2str(Phi)+";DPHI="+num2str(Dphi)+"
;WIDTH=0;SIDE="+side+";QCENTER=0;QDELTA=0;"
    String/G root:myGlobals:Protocols:gAvgInfoStr=temp
    //setup a "fake protocol" wave, sice I have no idea of the current sta
te of the data
    Make/O/T/N=8 root:myGlobals:Protocols:fakeProtocol
    Wave/T fakeProtocol = $"root:myGlobals:Protocols:fakeProtocol"
    String junk="Unknown file from Average_Panel"
    fakeProtocol[0] = junk
    fakeProtocol[1] = junk
    fakeProtocol[2] = junk
    fakeProtocol[3] = junk
    fakeProtocol[4] = junk
    fakeProtocol[5] = junk
    fakeProtocol[6] = junk
    fakeProtocol[7] = temp
    //set the global
    String/G root:myGlobals:Protocols:gProtoStr = "fakeProtocol"

    CircularAverageTo1D(type)
    if (useXMLOutput == 1)
        WriteXMLWaves_W_Protocol(type,path+prefix+num2
str(Phi),0)
    else
        WriteWaves_W_Protocol(type,path+prefix+num2str
(Phi),0)      //"" is an empty path, I will force a dialog
    endif
    i+=1
    while(phi<Phi_max)
    //Print out info
    print "=====DONE====="
    print "select next line and hit enter to run again"
    print "MultSectAvg()"
    print ""//for new line

    print "Values used:"
    print "Phi_initial: "+num2str(Phi_initial)

```

```

print "Phi_step: "+num2str(Phi_step)
print "DPhi: "+num2str(DPhi)
print "Phi_max: " + num2str(Phi_max)
print "prefix: "+prefix
print ""//for new line
print "Saved in: "+path
End

Function MultAnnulAvg()

//USER VARIABLE SELECTION
//create variables with default values
Variable Q_initial=.005
Variable Q_step=.01
Variable Q_max=.11
Variable pixels=10
String prefix="[FIELD]_[TEMP]_[DATE]"
//prompt user to change values
Prompt Q_initial,"First Q Value (Float)"
Prompt Q_step,"Increment in QCenter (Float)"
Prompt Q_max,"Maximum Q Center Value (Float)"
Prompt pixels,"QDelta (Pixels) (Integer)"
Prompt prefix,"Output File Prefix (string) - KEEP THE QUOTES"
DoPrompt "Enter Below values, Current Values are Defaults",prefix,Q_initial,Q_
step,Q_max,pixels //Keep Prefix First as this is what will be modified every time so i
ts nice for user this way
if(V_Flag)
    Abort "You Cancelled - Ouch, I have feelings you know...."
endif
//END USER VARIABLE SELCTION

// need next two lines or wont work
SVAR type=root:myGlobals:gDataDisplayType
NVAR useXMLOutput = root:Packages:NIST:gXML_Write

String path=MultAvgSetUp()//set path and do some other set up

Variable i=0 //variable for loop
do //Loop over Q values taking an annular average at each step
    Variable QCENTER = Q_initial + Q_step*(i)
    //build the string that the averaging routine is looking for
    String temp="AVTYPE=Annular;PHI=0;DPhi=0;WIDTH=0;SIDE=both;QCENTER="+n
um2str(QCENTER)+";QDELTa="+num2str(pixels)+";"
    String/G root:myGlobals:Protocols:gAvgInfoStr=temp //set global variab
le

    //setup a "fake protocol" wave, sice I have no idea of the current sta
te of the data
    Make/O/T/N=8 root:myGlobals:Protocols:fakeProtocol
    Wave/T fakeProtocol = $"root:myGlobals:Protocols:fakeProtocol"
    String junk="Unknown file from Average_Panel"
    fakeProtocol[0] = junk
    fakeProtocol[1] = junk
    fakeProtocol[2] = junk
    fakeProtocol[3] = junk
    fakeProtocol[4] = junk
    fakeProtocol[5] = junk
    fakeProtocol[6] = junk
    fakeProtocol[7] = temp
    //set the global
    String/G root:myGlobals:Protocols:gProtoStr = "fakeProtocol"
    AnnularAverageToID(type) //do avg
    WritePhiave_W_Protocol(type,path+prefix+"_AN_"+num2str(1000*QCENTER),0
)// save average -"" is an empty path, 1 will force a dialog - 0 Saves to path.
    i+=1
    while(QCENTER<Q_max)
    //Print out info
    print "=====DONE====="

```

```

print "select next line and hit enter to run again"
print "MultAnnulAvg()"
print ""//for new line
print "Values used:"
print "Q_initial: "+num2str(Q_initial)
print "Q_step: "+num2str(Q_step)
print "Q_max: "+num2str(Q_max)
print "Q Delta (pixels): " + num2str(pixels)
print "prefix: "+prefix
print ""//for new line
print "Saved in: "+path

End

//Utility Functions for things that are repeated in different Mult Avg Functions
Function/S MultAvgSetUp()
    //Things from main average panel that are important to setting up the average
    //SAVE PATH IS CHOSEN IN THIS FUNCTION
    //returns the path chosen by the user
    SVAR type=root:myGlobals:gDataDisplayType
    NVAR useXMLOutput = root:Packages:NIST:gXML_Write
    //Check for logscale data in "type" folder
    String dest = "root:Packages:NIST:"+type
    NVAR isLogScale = $(dest + ":IsLogScale")
    Variable wasLogScale=isLogScale
    if(isLogScale)
        ConvertFolderToLinearScale(type)
    Endif
    //set data folder back to root (redundant)
    SetDataFolder root:

    //CHOOSE SAVING FOLDER
    PickPath()
    PathInfo catPathName

    return S_Path //return path chosen by user
End

=====NICE MENU=====
=====

Function AnnularButtonProc(ba) : ButtonControl
    STRUCT WMButtonAction &ba

    switch( ba.eventCode )
        case 2: // mouse up
            MultAnnulAvg()
            break
        case -1: // control being killed
            break
    endswitch

    return 0
End
Function SectorButtonProc(ba) : ButtonControl
    STRUCT WMButtonAction &ba

    switch( ba.eventCode )
        case 2: // mouse up
            MultSectAvg()
            break
        case -1: // control being killed
            break
    endswitch

    return 0
End

```

```

Function CalcAllButtonProc(ba) : ButtonControl
    STRUCT WMButtonAction &ba

        switch( ba.eventCode )
            case 2: // mouse up
                calcAll()
                break
            case -1: // control being killed
                break
        endswitch

        return 0
End
Function OC_Macros_DoneButton(ctrlName) : ButtonControl

    String ctrlName
    Abort "UNIMPLEMENTED"
    // This is not implemented because once you close it you aren't able to reopen
    it for some reason.
//    DoWindow/K OC_Macros
//    SetDataFolder root:
End

Window OC_Macros() : Panel
//Issues:
//If multiple panels are opened then teh kill window will only kill the first p
anel

    PauseUpdate; Silent 1           // building window...
    Variable GoldRat=1.618 //golden ratio - overdesign forever
    Variable YLength = 200 // base all other lengths of this and golden ratio

    //Making Frame
    Variable X1 = 1200 //top left corner X
    Variable Y1 = 10 //top left corner Y
    NewPanel /W=(X1,Y1,GoldRat*YLength+X1,YLength+Y1) as "Oberlin SANS Macros"
    ModifyPanel frameStyle=2 //dope indented walls
    ModifyPanel fixedSize=1 //I DECIDE THE SIZE - NOT THE USER grrrr
    variable rgbFactor =65535/255 //cbRGB is some weird rgb system
    ModifyPanel cbRGB=(176*rgbFactor,196*rgbFactor,222*rgbFactor) //color name is
    lightsteelblue in case you were wondering

    Variable ButtonHeight=YLength/(GoldRat*GoldRat)
    Variable ButtonLength=YLength/GoldRat

    //button insets
    Variable YInset=6
    Variable XInset=10

    Variable YButtonGap=YLength-2*YInset-2*ButtonHeight
    Variable XButtonGap=YLength*GoldRat-2*ButtonLength-2*XInset
    Variable LowerButtonY = YLength-YInset-ButtonHeight
    Variable RightButtonX = XInset+ButtonHeight*GoldRat+XButtonGap
//make buttons
    Button AnnulAvgBtn,pos={XInset,YInset},size={ButtonLength,ButtonHeight},proc=
AnnularButtonProc,title="Multiple Annular Avg"
    Button SectAvgBtn,pos={RightButtonX,YInset},size={ButtonLength,ButtonHeight},p
roc= SectorButtonProc,title="Multiple Sector Avg"
    Button MultBCalc,pos={XInset,LowerButtonY},size={ButtonLength,ButtonHeight},pr
oc=CalcAllButtonProc,title="Calc Components"
    Button Done,pos={RightButtonX,LowerButtonY},size={ButtonLength,ButtonHeight/Go
ldRat},proc=OC_Macros_DoneButton,title="Close Panel"
EndMacro

//Added By Ian Hunt-Isaak ihuntisaak@oberlin (through may 2017) Permanent: ianhuntisaak@
gmail.com
//Last Modified Sept 26 2015

```

```
// MultAnnAvg() Performs Annular Averages at multiple Q values on the result of a workfile math operation.  
// MultSectAvg() Performs Sector Averages at multiple Phi values on the result of a workfile math operation.  
  
#pragma rtGlobals=3 // Use modern global access method and strict wave access.  
  
Function calcAll()  
    PickPath()  
    PathInfo catPathName  
    String path = S_Path  
    String prefix = extractPrefix(path)  
    print path  
    print prefix  
    calcN(path,prefix)  
    calcZ(path,prefix)  
    calcX1(path,prefix)  
    calcX2(path,prefix,90)  
    calcY(path,prefix)  
    calcYZ(path,prefix)  
    calcRatio(path,prefix)  
end  
  
Function calcN(path, prefix)  
    String path //C:Users:Magnetic:Hillary:TestFolder  
    String prefix //HF_10_HQ  
    String pathPre = path+prefix  
    print pathPre  
    ASC_Math(pathPre+"_DD.asc",pathPre+"_UU.asc", "+")  
    String outName = "N_"+prefix  
    secAvg(0,10,"both", path, outName)  
end  
  
Function calcZ(path, prefix)  
    String path  
    String prefix  
    String pathPre = path+prefix  
    ASC_Math(pathPre+"_UD.asc",pathPre+"_DU.asc", "+")  
  
    String outName = "Z_"+prefix  
    secAvg(90,10,"both", path, outName)  
end  
  
Function calcX1(path, prefix)  
    String path  
    String prefix  
    String pathPre = path+prefix  
    ASC_Math(pathPre+"_DD.asc",pathPre+"_UU.asc", "+")  
    secAvg(90,10,"both",path, prefix+_A90")  
    secAvg(0,10,"both", path, prefix+_A0")  
    loadFile(path,prefix+_A90")  
    loadFile(path,prefix+_A0")  
    String outName=_X1_+prefix  
    SubtractDataSets(prefix+_A90",prefix+_A0", 1, outName)  
    fReWrite1DData_noPrompt(outName,"tab","CRLF")  
end  
  
Function calcX2(path, prefix, phi)  
    String path
```

```

String prefix
Variable phi

String pathPre=path+prefix
String A_Data=prefix+"_A90"
String B_Data=prefix+"_B"+num2str(phi)

ASC_Math(pathPre+"_DD.asc",pathPre+"_UU.asc", "+")
secAvg(90,10,"both",path, A_Data)
ASC_Math(pathPre+"_DD.asc",pathPre+"_UU.asc", "-")
secAvg(phi,10,"both", path, B_Data)
loadFile(path,A_Data)
loadFile(path,B_Data)

MultiplyDataSets(B_Data,B_Data,1,"temp")
variable factor = sin(phi*pi/180)^4

String outName = "X2_"+prefix
if(phi==90)
    // For consistency wih old work
    DivideDataSets("temp",A_Data,4*factor,outName)
    fReWrite1DData_noPrompt(outName,"tab","CRLF")
else
    DivideDataSets("temp",A_Data,4*factor,outName+"_"+num2str(phi))
    fReWrite1DData_noPrompt(outName+"_"+num2str(phi),"tab","CRLF")
endif
end

Function calcYZ(path, prefix)
String path
String prefix
String pathPre = path+prefix

ASC_Math(pathPre+"_UD.asc",pathPre+"_DU.asc", "+")

String outName = "YZ_"+prefix
secAvg(0,10,"both", path, outName)
end

Function calcY(path, prefix)
String path
String prefix
String pathPre = path+prefix

ASC_Math(pathPre+"_UD.asc",pathPre+"_DU.asc", "+")
secAvg(0,10,"both",path, prefix+"_C0")
secAvg(90,10,"both", path, prefix+"_C90")

loadFile(path,prefix+"_C0")
loadFile(path,prefix+"_C90")

String outName="Y_"+prefix
SubtractDataSets(prefix+"_C0",prefix+"_C90", 1, outName)
fReWrite1DData_noPrompt(outName,"tab","CRLF")
End
Function calcRatio(path, prefix)
// Calculate the ratio of sec90/sec0 sec90=sector avg at 90 deg
String path
String prefix

String pathPre=path+prefix
String Z_Data=prefix+"_C90"
String YZ_Data=prefix+"_C0"

ASC_Math(pathPre+"_DU.asc",pathPre+"_UD.asc", "+")
secAvg(90,10,"both",path, Z_Data)
ASC_Math(pathPre+"_DU.asc",pathPre+"_UD.asc", "-")

```

```

secAvg(0,10,"both", path, YZ_Data)
loadFile(path,A_Data)
loadFile(path,B_Data)

String outName = "ratio_"+prefix
DivideDataSets(YZ_Data,Z_Data,1,outName)
fReWrite1DData_noPrompt(outName,"tab","CRLF")

End

//++++++Utility Functions+++++++
Function/S extractPrefix(input)
    //Extracts just the prefix from a path to condition
    //Assumes path is of the form:
    //
    // extractPrefix ("C:Users:Ian: HF_10 : HF_10_HQ:")
    // should return "HF_10_HQ"

    String input
    String prefix = ""
    Variable len = strlen(input)
    Variable pos = strSearch(input,":",len-2,1) //strSearch(str, findThisStr, start[, options]), 1 is search backwards
    if(strsearch(input[pos+1,len-2],"_",0)==-1)
        //If guess string contains no underscores assume we're in a new polarization
        //
        // i.e. ....:MF_200_HQ:p9:
        Variable pos2 = strSearch(input,":",pos-1,1)
        String condInfo = input[pos2+1,pos-1]
        Variable firstUnder = strSearch(condInfo,"_",0)
        prefix = condInfo[0(firstUnder)] + input[pos+1,len-2]+condInfo[firstUnder,strlen(condInfo)]
    else
        prefix = input[pos+1,len-2]
    endif

    prompt prefix,"Prefix"
    DoPrompt "If nothing entered will guess based on path",prefix
    if(V_Flag)
        Abort "You Cancelled - Ouch, I have feelings you know...."
    endif

    return prefix
end

Function loadFile(location,filestr)
    String filestr,location
    String path=location+filestr
    Execute "A_LoadOneDDataWithName(\\""+path+"\\", "+num2str(0)+")"
End
//-----
Function ASC_Math(path1,path2,oper)
    //Function allows calling without multiplying data with constants
    String path1,path2,oper
    ASC_Math_consts(path1,path2,oper,1,1)
End

Function ASC_Math_consts(path1,path2,oper,const1,const2)
    // WorkMath panel needs to be open in order for there to be the proper data folders
    // Performs arithmetic on ASC files.
    String path1
    String path2
    String oper
    Variable const1, const2

```

```

String str1,str2,dest = "Result"
String pathStr,workMathStr="WorkMath:"
if( DataFolderExists(workMathStr) )
    // good workmath file is up
else
    Execute "Init_WorkMath()"
endif
//set #1
Load_NamedASC_File(path1,workMathStr+"File_1")

NVAR pixelsX = root:myGlobals:gNPixelsX           //OK, location is correct
NVAR pixelsY = root:myGlobals:gNPixelsY

WAVE/Z data1=$( "root:Packages:NIST:"+workMathStr+"File_1:linear_data")
WAVE/Z err1=$( "root:Packages:NIST:"+workMathStr+"File_1:linear_data_error")

//Load set #2
Load_NamedASC_File(path2,workMathStr+"File_2")
WAVE/Z data2=$( "root:Packages:NIST:"+workMathStr+"File_2:linear_data")
WAVE/Z err2=$( "root:Packages:NIST:"+workMathStr+"File_2:linear_data_error")

//copy contents of str1 folder to dest and create the wave ref (it will exist)
CopyWorkContents(workMathStr+"File_1",workMathStr+dest)
WAVE/Z destData=$( "root:Packages:NIST:"+workMathStr+dest+":linear_data")
WAVE/Z destData_log=$( "root:Packages:NIST:"+workMathStr+dest+":data")
WAVE/Z destErr=$( "root:Packages:NIST:"+workMathStr+dest+":linear_data_error")

strswitch(oper)
    case "*":
        destData = const1*data1 * const2*data2
        destErr = const1^2*const2^2*(err1^2*data2^2 + err2^2*data1^2)
        destErr = sqrt(destErr)
        break
    case "-":
        destData = const1*data1 - const2*data2
        destErr = const1^2*err1^2 + const2^2*err2^2
        destErr = sqrt(destErr)
        break
    case "/":
        destData = (const1*data1) / (const2*data2)
        destErr = const1^2/const2^2*(err1^2/data2^2 + err2^2*data1^2/d
ata2^4)
        destErr = sqrt(destErr)
        break
    case "+":
        destData = const1*data1 + const2*data2
        destErr = const1^2*err1^2 + const2^2*err2^2
        destErr = sqrt(destErr)
        break
endswitch

destData_log = log(destData)           //for display
//show the result
WorkMath_Display_PopMenuProc("",0,"Result")
End

//-----
Function secAvg(Phi, Dphi, side,path,prefix)

    //If no input for saving - default is to save
    Variable Phi,Dphi
    String side, prefix, path
    secAvg_saveOption(Phi,Dphi,side,path,prefix,1)
End

Function secAvg_saveOption(Phi,Dphi,side,path,prefix,doSave)
    // for taking a sector average of whatever is up in the workfile math panel
    // Will fail if there is no result of a workfile math function up
    Variable Phi

```

```
Variable Dphi
String side
String prefix
String path
Variable doSave //1 for save - anything else for not save

// need next two lines or wont work
SVAR type=root:myGlobals:gDataDisplayType
NVAR useXMLOutput = root:Packages:NIST:gXML_Write

String dest = "root:Packages:NIST:"+type
NVAR isLogScale = $(dest + ":gIsLogScale")
Variable wasLogScale=isLogScale
if(isLogScale)
    ConvertFolderToLinearScale(type)
Endif
//set data folder back to root (redundant)
SetDataFolder root:

String temp="AVTYPE=Sector;PHI="+num2str(Phi)+";Dphi="+num2str(Dphi)+";WIDTH=0
;SIDE="+side+";QCENTER=0;QDELTA=0;"
String/G root:myGlobals:Protocols:gAvgInfoStr=temp
//setup a "fake protocol" wave, sice I have no idea of the current state of th
e data
Make/O/T/N=8 root:myGlobals:Protocols:fakeProtocol
Wave/T fakeProtocol = $"root:myGlobals:Protocols:fakeProtocol"
String junk="Unknown file from Average_Panel"
fakeProtocol[0] = junk
fakeProtocol[1] = junk
fakeProtocol[2] = junk
fakeProtocol[3] = junk
fakeProtocol[4] = junk
fakeProtocol[5] = junk
fakeProtocol[6] = junk
fakeProtocol[7] = temp
//set the global
String/G root:myGlobals:Protocols:gProtoStr = "fakeProtocol"

CircularAverageToID(type)
if(doSave==1)
    WriteWaves_W_Protocol(type,path+prefix,0)
endif
End
```

Bibliography

- [1] Srikanth Singamaneni et al. “Magnetic nanoparticles: recent advances in synthesis, self-assembly and applications”. In: *Journal of Materials Chemistry* 21.42 (Oct. 18, 2011), pp. 16819–16845. ISSN: 1364-5501. DOI: 10.1039/C1JM11845E. URL: <http://pubs.rsc.org/en/content/articlelanding/2011/jm/c1jm11845e> (visited on 03/31/2017) (cit. on p. 1).
- [2] “Novel structures and physics of nanomagnets (invited)”. In: *Journal of Applied Physics* 117.17 (Mar. 11, 2015), p. 172609. ISSN: 0021-8979. DOI: 10.1063/1.4914339. URL: <http://aip.scitation.org/doi/10.1063/1.4914339> (visited on 03/31/2017) (cit. on p. 1).
- [3] K O’Grady and H Laidler. “The limits to magnetic recording — media considerations”. In: *Journal of Magnetism and Magnetic Materials* 200.1 (Oct. 1999), pp. 616–633. ISSN: 0304-8853. DOI: 10.1016/S0304-8853(99)00499-0. URL: <http://www.sciencedirect.com/science/article/pii/S0304885399004990> (visited on 03/22/2017) (cit. on p. 2).
- [4] Fabian M. Koehler et al. “Magnetic EDTA: coupling heavy metal chelators to metal nanomagnets for rapid removal of cadmium, lead and copper from contaminated water”. In: 32 (Aug. 3, 2009), pp. 4862–4864. ISSN: 1364-548X. DOI: 10.1039/B909447D. URL: <http://pubs.rsc.org/en/content/articlelanding/2009/cc/b909447d> (visited on 03/22/2017) (cit. on p. 2).
- [5] R Taylor et al. “Small particles, big impacts: A review of the diverse applications of nanofluids”. In: *Journal of Applied Physics* 113.1 (Jan. 2, 2013), p. 011301. ISSN: 0021-8979. DOI: 10.1063/1.4754271. URL: <http://aip.scitation.org/doi/10.1063/1.4754271> (visited on 03/31/2017) (cit. on p. 2).

BIBLIOGRAPHY

- [6] S. Odenbach. “Recent progress in magnetic fluid research”. In: *Journal of Physics: Condensed Matter* 16.32 (2004), R1135. ISSN: 0953-8984. DOI: 10.1088/0953-8984/16/32/R02. URL: <http://stacks.iop.org/0953-8984/16/i=32/a=R02> (visited on 03/31/2017) (cit. on p. 2).
- [7] Christoph Alexiou et al. “Targeting cancer cells: magnetic nanoparticles as drug carriers”. In: *European Biophysics Journal* 35.5 (May 1, 2006), pp. 446–450. ISSN: 0175-7571, 1432-1017. DOI: 10.1007/s00249-006-0042-1. URL: <https://link.springer.com/article/10.1007/s00249-006-0042-1> (visited on 03/22/2017) (cit. on p. 2).
- [8] Q. A. Pankhurst et al. “Progress in applications of magnetic nanoparticles in biomedicine”. In: *Journal of Physics D: Applied Physics* 42.22 (2009), p. 224001. ISSN: 0022-3727. DOI: 10.1088/0022-3727/42/22/224001. URL: <http://stacks.iop.org/0022-3727/42/i=22/a=224001> (visited on 03/22/2017) (cit. on p. 2).
- [9] Christine Rümenapp, Bernhard Gleich, and Axel Haase. “Magnetic Nanoparticles in Magnetic Resonance Imaging and Diagnostics”. In: *Pharmaceutical Research* 29.5 (May 1, 2012), pp. 1165–1179. ISSN: 0724-8741, 1573-904X. DOI: 10.1007/s11095-012-0711-y. URL: <https://link.springer.com/article/10.1007/s11095-012-0711-y> (visited on 03/22/2017) (cit. on p. 2).
- [10] L. Berger et al. “Ferromagnetic nanoparticles with strong surface anisotropy: Spin structures and magnetization processes”. In: *Physical Review B* 77.10 (Mar. 24, 2008), p. 104431. DOI: 10.1103/PhysRevB.77.104431. URL: <http://link.aps.org/doi/10.1103/PhysRevB.77.104431> (visited on 03/16/2017) (cit. on pp. 3, 4).
- [11] R. H. Kodama and A. E. Berkowitz. “Atomic-scale magnetic modeling of oxide nanoparticles”. In: *Physical Review B* 59.9 (Mar. 1, 1999), pp. 6321–6336. DOI: 10.1103/PhysRevB.59.6321. URL: <http://link.aps.org/doi/10.1103/PhysRevB.59.6321> (visited on 03/22/2017) (cit. on p. 3).
- [12] R. H. Kodama. “Magnetic nanoparticles”. In: *Journal of Magnetism and Magnetic Materials* 200.1 (Oct. 1999), pp. 359–372. ISSN: 0304-8853. DOI: 10.1016/S0304-8853(99)00347-9. URL: <http://www.sciencedirect.com/science/article/pii/S0304885399003479> (visited on 03/17/2017).

BIBLIOGRAPHY

- [13] K Hasselbach, C Veauvy, and D Mailly. “MicroSQUID magnetometry and magnetic imaging”. In: *Physica C: Superconductivity* 332.1 (May 2000), pp. 140–147. ISSN: 0921-4534. DOI: 10.1016/S0921-4534(99)00657-7. URL: <http://www.sciencedirect.com/science/article/pii/S0921453499006577> (visited on 03/22/2017) (cit. on p. 5).
- [14] J.-P. Cleuziou et al. “Carbon nanotube superconducting quantum interference device”. In: *Nature Nanotechnology* 1.1 (Oct. 2006), pp. 53–59. ISSN: 1748-3387. DOI: 10.1038/nnano.2006.54. URL: <http://www.nature.com/nnano/journal/v1/n1/full/nnano.2006.54.html> (visited on 03/22/2017) (cit. on p. 5).
- [15] R. Wiesendanger et al. “Fundamental studies of magnetism down to the atomic scale: present status and future perspectives of spin-polarized scanning tunneling microscopy”. In: *Journal of Magnetism and Magnetic Materials*. Proceedings of the International Conference on Magnetism (ICM 2003) 272–276, Part 3 (May 2004), pp. 2115–2120. ISSN: 0304-8853. DOI: 10.1016/j.jmmm.2003.12.817. URL: <http://www.sciencedirect.com/science/article/pii/S0304885303017803> (visited on 03/31/2017) (cit. on p. 5).
- [16] P. Křišťan et al. “Structure of Iron Oxide Nanoparticles Studied by ^{57}Fe NMR”. In: *Acta Physica Polonica A* 126.1 (July 2014), pp. 138–139. ISSN: 0587-4246, 1898-794X. DOI: 10.12693/APhysPolA.126.138. URL: <http://przyrbwn.icm.edu.pl/APP/PDF/126/a126z1p065.pdf> (visited on 03/22/2017) (cit. on p. 5).
- [17] Claude Berthier, Laurent P. Levy, and Gerard Martinez. *High Magnetic Fields: Applications in Condensed Matter Physics and Spectroscopy*. Google-Books-ID: egZqCQAAQBAJ. Springer, Jan. 11, 2008. 503 pp. ISBN: 978-3-540-45649-0 (cit. on p. 5).
- [18] B. Kalska-Szostko, D. Satuła, and W. Olszewski. “Mössbauer spectroscopy studies of the magnetic properties of ferrite nanoparticles”. In: *Current Applied Physics* 15.3 (Mar. 2015), pp. 226–231. ISSN: 15671739. DOI: 10.1016/j.cap.2014.12.011. URL: <http://linkinghub.elsevier.com/retrieve/pii/S1567173914003964> (visited on 03/22/2017) (cit. on p. 5).
- [19] D S Sivia. *Elementary scattering theory: for X-ray and neutron users*. Oxford: Oxford Univ. Press, 2011 (cit. on p. 6).

BIBLIOGRAPHY

- [20] U Keiderling et al. “SANS polarization analysis at V4 SANS instrument of HMI Berlin”. In: *Measurement Science and Technology* 19.3 (Mar. 1, 2008), p. 034009. ISSN: 0957-0233, 1361-6501. DOI: 10.1088/0957-0233/19/3/034009. URL: <http://stacks.iop.org/0957-0233/19/i=3/a=034009?key=crossref.7ec4f4e0e006c1f012ad370b349d8a66> (visited on 03/20/2017) (cit. on p. 6).
- [21] Albrecht Wiedenmann. “Small-angle neutron scattering investigations of magnetic nanostructures and interfaces using polarized neutrons”. In: *Physica B: Condensed Matter* 297.1 (2001), pp. 226–233. URL: <http://www.sciencedirect.com/science/article/pii/S0921452600008723> (visited on 03/20/2017) (cit. on p. 6).
- [22] Albrecht Wiedenmann. “Polarized SANS for probing magnetic nanostructures”. In: *Physica B: Condensed Matter* 356.1 (Feb. 2005), pp. 246–253. ISSN: 09214526. DOI: 10.1016/j.physb.2004.10.085. URL: <http://linkinghub.elsevier.com/retrieve/pii/S0921452604011044> (visited on 03/20/2017) (cit. on p. 6).
- [23] Kathryn Hasz. “Polarization Analyzed Small Angle Neutron Scattering of Ferrite Nanoparticles”. PhD thesis. Oberlin College, 2014. URL: http://rave.ohiolink.edu/etdc/view?acc_num=oberlin1400837839 (visited on 09/08/2016) (cit. on pp. 8–10, 21, 33).
- [24] Ryan Anderson Booth. “Inter- and Intraparticle Interactions in Magnetic Nanoparticle Systems”. PhD thesis. CARNEGIE MELLON UNIVERSITY, 2012. URL: <http://gradworks.umi.com/35/33/3533450.html> (visited on 03/27/2017) (cit. on pp. 10, 30–32).
- [25] S.A. Majetich et al. “Magnetic nanoparticles and magnetocrystalline anisotropy”. In: *Nanostructured Materials* 9.1 (Jan. 1997), pp. 291–300. ISSN: 09659773. DOI: 10.1016/S0965-9773(97)90069-6. URL: <http://linkinghub.elsevier.com/retrieve/pii/S0965977397900696> (visited on 01/12/2017) (cit. on pp. 10, 12).
- [26] David J. Griffiths. *Introduction to Electrodynamics*. 4 edition. Boston: Pearson, Oct. 6, 2012. 624 pp. ISBN: 978-0-321-85656-2 (cit. on p. 10).
- [27] K. Hasz et al. “Particle moment canting in CoFe₂O₄ nanoparticles”. In: *Physical Review B* 90.18 (Nov. 19, 2014). ISSN: 1098-0121, 1550-235X. DOI: 10.1103/PhysRevB.90.180405. URL: <http://link.aps.org/doi/10.1103/PhysRevB.90.180405> (visited on 09/08/2016) (cit. on pp. 11, 22, 23).

BIBLIOGRAPHY

- [28] Sōshin Chikazumi. *Physics of magnetism*. Google-Books-ID: 9sjvAAAA-MAAJ. Wiley, 1964. 576 pp. (cit. on pp. 11, 23).
- [29] R. F. Penoyer and M. W. Shafer. “On the Magnetic Anisotropy in Manganese-Iron Spinels”. In: *Journal of Applied Physics* 30.4 (Apr. 1959), S315–S316. ISSN: 0021-8979, 1089-7550. DOI: 10.1063/1.2185951. URL: <http://aip.scitation.org/doi/10.1063/1.2185951> (visited on 03/17/2017) (cit. on p. 11).
- [30] Joel I. Gersten and Frederick W. Smith. *The Physics and Chemistry of Materials*. 1 edition. New York: Wiley-Interscience, June 25, 2001. 856 pp. ISBN: 978-0-471-05794-9 (cit. on pp. 11, 12).
- [31] Richard M. Bozorth. *Ferromagnetism*. Piscataway, N.J: Wiley-IEEE Press, Aug. 27, 1993. 992 pp. ISBN: 978-0-7803-1032-2 (cit. on pp. 11, 23).
- [32] T. Chatterji. *Neutron Scattering from Magnetic Materials*. Gulf Professional Publishing, 2005 (cit. on p. 15).
- [33] Kathryn Krycka et al. “Polarization-analyzed small-angle neutron scattering. II. Mathematical angular analysis”. In: *Journal of Applied Crystallography* 45.3 (2012), pp. 554–565. URL: <http://scripts.iucr.org/cgi-bin/paper?ks5292> (visited on 09/10/2016) (cit. on pp. 16–19).
- [34] R. M. Moon, T. Riste, and W. C. Koehler. “Polarization analysis of thermal-neutron scattering”. In: *Physical Review* 181.2 (1969), p. 920. URL: <https://journals.aps.org/pr/abstract/10.1103/PhysRev.181.920> (visited on 03/17/2017) (cit. on p. 16).
- [35] W.C. Chen et al. “Applications of 3He neutron spin filters at the NCNR”. In: *Physica B: Condensed Matter* 404.17 (Sept. 2009), pp. 2663–2666. ISSN: 09214526. DOI: 10.1016/j.physb.2009.06.040. URL: <http://linkinghub.elsevier.com/retrieve/pii/S0921452609004001> (visited on 03/20/2017) (cit. on p. 17).
- [36] W. C. Chen et al. “Polarized ^3He cell development and application at NIST”. In: *Journal of Physics: Conference Series* 294.1 (2011), p. 012003. ISSN: 1742-6596. DOI: 10.1088/1742-6596/294/1/012003. URL: <http://stacks.iop.org/1742-6596/294/i=1/a=012003> (visited on 03/27/2017) (cit. on p. 17).

BIBLIOGRAPHY

- [37] C. B. Fu et al. “A wide angle neutron spin filter system using polarized ^3He ”. In: *Physica B: Condensed Matter*. Proceedings of the 8th International Workshop on Polarised Neutrons for Condensed Matter Investigation 406.12 (June 2011), pp. 2419–2423. ISSN: 0921-4526. DOI: 10.1016/j.physb.2010.10.002. URL: <http://www.sciencedirect.com/science/article/pii/S0921452610009348> (visited on 03/27/2017) (cit. on p. 17).
- [38] Kathryn Krycka et al. “Polarization-analyzed small-angle neutron scattering. I. Polarized data reduction using *Pol-Corr*”. In: *Journal of Applied Crystallography* 45.3 (June 1, 2012), pp. 546–553. ISSN: 0021-8898. DOI: 10.1107/S0021889812003445. URL: <http://scripts.iucr.org/cgi-bin/paper?S0021889812003445> (visited on 09/10/2016) (cit. on p. 17).
- [39] K.L. Krycka et al. “Resolving 3D magnetism in nanoparticles using polarization analyzed SANS”. In: *Physica B: Condensed Matter* 404.17 (Sept. 2009), pp. 2561–2564. ISSN: 09214526. DOI: 10.1016/j.physb.2009.06.024. URL: <http://linkinghub.elsevier.com/retrieve/pii/S0921452609003743> (visited on 09/08/2016) (cit. on pp. 20, 31, 33).
- [40] K. L. Krycka et al. “Core-Shell Magnetic Morphology of Structurally Uniform Magnetite Nanoparticles”. In: *Physical Review Letters* 104.20 (May 19, 2010). ISSN: 0031-9007, 1079-7114. DOI: 10.1103/PhysRevLett.104.207203. URL: <http://link.aps.org/doi/10.1103/PhysRevLett.104.207203> (visited on 09/08/2016) (cit. on pp. 20, 21).
- [41] K. L. Krycka et al. “Origin of Surface Canting within Fe_3O_4 Nanoparticles”. In: *Physical Review Letters* 113.14 (Oct. 2, 2014). ISSN: 0031-9007, 1079-7114. DOI: 10.1103/PhysRevLett.113.147203. URL: <http://link.aps.org/doi/10.1103/PhysRevLett.113.147203> (visited on 09/08/2016) (cit. on pp. 20, 22, 23).
- [42] Adam J. Rondinone, Anna C. S. Samia, and Z. John Zhang. “Characterizing the magnetic anisotropy constant of spinel cobalt ferrite nanoparticles”. In: *Applied Physics Letters* 76.24 (June 12, 2000), pp. 3624–3626. ISSN: 0003-6951, 1077-3118. DOI: 10.1063/1.126727. URL: <http://aip.scitation.org/doi/10.1063/1.126727> (visited on 03/17/2017) (cit. on p. 23).

BIBLIOGRAPHY

- [43] Julius M. Hastings and Lester M. Corliss. “Neutron Diffraction Study of Manganese Ferrite”. In: *Physical Review* 104.2 (Oct. 15, 1956), pp. 328–331. DOI: 10.1103/PhysRev.104.328. URL: <http://link.aps.org/doi/10.1103/PhysRev.104.328> (visited on 03/27/2017) (cit. on p. 23).
- [44] RC O’Handley. *Modern Magnetic Materials*. Wiley, 2000 (cit. on p. 24).
- [45] Shouheng Sun et al. “Monodisperse MFe₂O₄ (M = Fe, Co, Mn) Nanoparticles”. In: *Journal of the American Chemical Society* 126.1 (Jan. 1, 2004), pp. 273–279. ISSN: 0002-7863. DOI: 10.1021/ja0380852. URL: <http://dx.doi.org/10.1021/ja0380852> (visited on 03/27/2017) (cit. on p. 25).
- [46] D. V. Talapin et al. “A New Approach to Crystallization of CdSe Nanoparticles into Ordered Three-Dimensional Superlattices”. In: *Advanced Materials* 13.24 (Dec. 1, 2001), pp. 1868–1871. ISSN: 1521-4095. DOI: 10.1002/1521-4095(200112)13:24<1868::AID-ADMA1868>3.0.CO;2-0. URL: [http://onlinelibrary.wiley.com/doi/10.1002/1521-4095\(200112\)13:24<1868::AID-ADMA1868>3.0.CO;2-0/abstract](http://onlinelibrary.wiley.com/doi/10.1002/1521-4095(200112)13:24<1868::AID-ADMA1868>3.0.CO;2-0/abstract) (visited on 03/27/2017) (cit. on p. 25).
- [47] *fcc paracrystal documentation*. Mar. 27, 2017. URL: http://www.sasview.org/docs/user/models/fcc_paracrystal.html (cit. on pp. 26, 42).
- [48] URL: <https://www.ncnr.nist.gov/> (visited on 03/20/2017) (cit. on p. 30).
- [49] Steven R. Kline. “Reduction and analysis of SANS and USANS data using IGOR Pro”. In: *Journal of Applied Crystallography* 39.6 (Dec. 1, 2006), pp. 895–900. ISSN: 0021-8898. DOI: 10.1107/S0021889806035059. URL: <http://scripts.iucr.org/cgi-bin/paper?S0021889806035059> (visited on 03/22/2017) (cit. on pp. 33, 36, 40).
- [50] *SasView*. URL: <http://www.sasview.org/> (cit. on p. 42).
- [51] Andreas Michels et al. “Micromagnetic simulation of magnetic small-angle neutron scattering from two-phase nanocomposites”. In: *Journal of Magnetism and Magnetic Materials* 350 (Jan. 2014), pp. 55–68. ISSN: 03048853. DOI: 10.1016/j.jmmm.2013.09.031. URL: <http://linkinghub.elsevier.com/retrieve/pii/S0304885313006902> (visited on 09/08/2016) (cit. on p. 47).

BIBLIOGRAPHY

- [52] Kathryn Krycka. personal communication (cit. on p. 49).
- [53] URL: https://www.ncnr.nist.gov/programs/sans/pdf/Seminar_2014_11_19_JBarker.pdf (cit. on pp. 58, 59).
- [54] E. Babcock et al. “In-situ SEOP polarizer and initial tests on a high flux neutron beam”. In: *Physica B: Condensed Matter* 404.17 (Sept. 1, 2009), pp. 2655–2658. ISSN: 0921-4526. DOI: 10.1016/j.physb.2009.06.041. URL: <http://www.sciencedirect.com/science/article/pii/S0921452609003986> (visited on 03/28/2017) (cit. on p. 59).
- [55] Gurvinder Singh et al. “Self-assembly of magnetite nanocubes into helical superstructures”. In: *Science* 345.6201 (Sept. 5, 2014), pp. 1149–1153. ISSN: 0036-8075, 1095-9203. DOI: 10.1126/science.1254132. URL: <http://science.sciencemag.org/content/345/6201/1149> (visited on 03/28/2017) (cit. on p. 59).